



Direct numerical simulation of evaporation and condensation with the geometric VOF method and a sharp-interface phase-change model

Lubomír Bureš^{a,b,*}, Yohei Sato^b

^a Swiss Federal Institute of Technology (EPFL), Lausanne 1015, Switzerland

^b Nuclear Energy and Safety, Paul Scherrer Institute, 5232 Villigen PSI, Switzerland

ARTICLE INFO

Article history:

Received 11 September 2020

Revised 9 March 2021

Accepted 15 March 2021

Available online 30 March 2021

Keywords:

Direct numerical simulation (DNS)

Volume-of-fluid (VOF)

Phase change

Mass transfer

Non-condensable gas

Interface tracking

Direct contact condensation

ABSTRACT

The paper describes a coupling of the geometric Volume-of-Fluid (VOF) method with a sharp-interface phase-change model for Cartesian and axisymmetric grids. Both the interfacial position and the temperature field are resolved with subgrid accuracy. Species transport with implicit diffusion is considered in the gas phase. The numerical implementation of the method developed here is described in detail, as well as its coupling with the incompressible Navier-Stokes solver PSI-BOIL, which features a hybrid, finite-volume/finite-difference approach based on a fixed, rectangular grid. Several verification cases have been undertaken to ensure correct implementation of the method in the code and to evaluate its performance. These include simulations of the Stefan problem, sucking problem and bubble growth in superheated liquid. In all cases, very good agreement with the analytical solution has been reached and grid convergence has been demonstrated. Simulations of evaporating and condensing rising bubbles, for which high-quality measured data are available, are also presented to serve as validation tests. Reasonable agreement of simulation results with experimental data has been recorded and applicability of the method to problems without inherent symmetry and featuring turbulence is shown. This work represents the first successful application of a geometric VOF method coupled with a sharp-interface phase-change model and species transport to non-trivial problems. The achieved performance of our algorithm in the verification and validation exercise represents an important step in the development of multiphase codes capable of accurately resolving complex three-dimensional multiphase flows.

© 2021 The Author(s). Published by Elsevier Ltd.

This is an open access article under the CC BY-NC-ND license (<http://creativecommons.org/licenses/by-nc-nd/4.0/>)

1. Introduction

Multiphase flow involving heat and mass transfer ranks among the most important industrial phenomena with fields of application including power generation, combustion engines and cooling and refrigeration systems, among others. Characteristics of boiling, evaporation and condensation significantly affect the design and performance of countless technological systems. This underlies the need for proper quantitative analysis of these processes and development of universal predictive tools, applicable in the whole range of multiphase flow configurations.

Computational Fluid Dynamics (CFD) have proven to be very successful for single-phase problems and their industrial use is now well-established. Conversely, the development of multiphase

CFD methods is still ongoing and their application is mostly limited to simple configurations [1]. Nevertheless, multiphase CFD simulations can bring insight into the dynamics of systems, for which a mechanistic description is not readily available. Furthermore, the extensive number of control variables in multiphase flows complicates the development of comprehensive experimental databases; thanks to the ability to freely manipulate simulation parameters, a validated CFD code can be used to complement the experimental data. Multiphase CFD codes can be especially useful for studying the basic physical phenomena governing the dynamics of problems involving phase change. This is the field of *Direct Numerical Simulation* (DNS), which attempts to resolve the equations of fluid continuum mechanics as they are, without the need for turbulence modelling and empirical interfacial closure laws.

A crucial element of multiphase CFD codes is the ability to capture the distribution of individual phases. For the purposes of DNS, the phasic interface must be accurately resolved using a high-fidelity Interface Tracking Method (ITM). A prominent example of an ITM is the Volume-of-Fluid (VOF) method [2], in which

* Corresponding author at: Nuclear Energy and Safety, Paul Scherrer Institute, 5232 Villigen PSI, Switzerland.

E-mail address: lubomir.bures@psi.ch (L. Bureš).

Glossary

ε	NCG volume fraction []
λ	thermal conductivity [W/mK]
μ	dynamic viscosity [Pa s]
ρ	mass density [kg/m ³]
σ	surface tension [N/m]
ϕ	liquid volume fraction []
φ_γ	interfacial area density [m ² /m ³]
C_p, c_p	isobaric volumetric [J/m ³ K] and specific [J/kg K] heat capacity
D	diffusion coefficient [m ² /s]
L	specific latent heat of phase transition [J/kg]
M	molar mass [kg/mol]
p	pressure [Pa] or [atm]
R_m	specific gas constant [J/kg K]
s_m	volumetric mass source [kg/m ³ s]
T	temperature [K]
u	velocity [m/s]
Re	Reynolds number, $Re = (u\rho d)/\mu$
CFL	Courant number, $CFL = (u\Delta t)/\Delta x$
CFD	computational fluid dynamics
DNS	direct numerical simulation
ITM	interface tracking method
NCG	non-condensable gas
VOF	volume-of-fluid

the phases are represented in terms of a cell-wise phasic volume-fraction function. In the original algebraic VOF approach the interfacial region had a finite thickness, determined by the underlying degree of grid refinement and covering several computational cells. In contrast, VOF with geometric advection techniques [3,4] can capture the interface in a sharp manner with subgrid accuracy using a geometrical reconstruction of the interface within the computational cells. Another major advantage of the VOF method is the possibility to formulate the algorithm in an inherently mass-conservative way without the need to resort to complex mass conservation enforcement schemes required by other popular ITMs, such as the Level Set method [5]. In the recent years, significant improvement has been achieved in the development of techniques for capturing interfacial characteristics using VOF, especially the surface tension force [6].

In the presence of phase change, the ITM must be complemented by a mass-transfer model of comparable fidelity. To match the accuracy and sharpness of the geometric VOF method for DNS purposes, a subgrid-accurate phase-change model must be considered. Several requirements can be formulated for such a general-purpose sharp-interface model:

1. Mass transfer should be implemented exactly at the phasic interface and conservation of mass must be exactly satisfied.
2. Position of the interface should be considered with subgrid accuracy.
3. No assumptions on the condition of the individual phases should be made (e.g. superheated, saturated).
4. It should be physics-based and free of empiricism.
5. It should not be restricted to problems involving species transport.
6. It should be applicable to 3D problems with complex interfacial topology.

A careful review of the single-species phase-change models, detailed e.g. by Kharangate and Mudawar [1], reveals that essentially the only available approach with the potential to fulfil the above requirements is to relate the phase-change rate to the interfacial

energy balance. With this method, the gradients of temperature must be calculated within the individual phases while taking into account the interfacial temperature, avoiding the imprecise mixture formulation. A challenging aspect of a subgrid-accurate model is the ability to consistently account for the interfacial position both during the solution of the energy transport equation and in mass transfer calculations. For example, a naive one-fluid formulation of the energy transport equation without corrective techniques results in the loss of information about temperature in cells featuring the interface and a subsequent loss of accuracy.

Geometric VOF with sharp-interface phase change has received some attention in the past. Pioneering work was conducted by the group of Welch [7–9], which focused on 2D simulations of film boiling; in these works, the irregular stencil for temperature gradients was used only during mass transfer rate calculations. Haelssig et al. [10] simulated two-dimensional counter-current flow with phase change using the approximate mixture formulation for treatment of near-interface cells. Ling et al. [11] and Sun et al. [12] simulated 2D boiling, while considering one of the phases to be saturated and approximating the temperature gradients in the interfacial cell by values at faces, sacrificing accuracy in the process. In the latter work, 2D axisymmetric bubble condensation was also presented. A 3D simulation of bubble-growth in a quiescent liquid was carried out by Akhtar and Kleis [13,14] using the mixture formulation, but the computed bubble shape was deformed and the growth rate was non-monotonic. A two-dimensional axisymmetric simulation of the same benchmark was successfully performed by Perez-Raya and Kandlikar [15] with only minor distortions of the temperature boundary layer observed. Aside of using mixture thermal diffusivities in interfacial cells, their method was able to capture the interface in a fully sharp manner. Perez-Raya and Kandlikar have successfully used their method for 2D axisymmetric simulations of nucleate boiling [16].

Recently, the importance of computing the phasic velocity needed for volume fraction advection in the presence of phase change in a divergence-free manner has been brought forward. To this end, an extrapolation method has been proposed by Malan et al. [17,18] and implemented in a solver combining the geometric VOF method with a sharp-interface phase-change model; advection of enthalpy was implemented using the mixture formulation. The two-fluid irregular-stencil discretisation of enthalpy diffusion of Sato and Niceno [19], originally developed for a smeared-interface ITM, was adopted. In the work of Malan et al. [17,18], the 3D simulation of bubble-growth in a quiescent liquid was successfully carried out. The authors have demonstrated convergence of their simulation to the analytical solution with first-order accuracy and the shapes of both the bubble and the temperature boundary layer have been shown to be preserved, at least in the direction normal to one of the coordinate axes. To the best of our knowledge, the work of Malan et al. constitutes the first verification of a three-dimensional geometric VOF method with a sharp-interface phase-change model; more complex problems have not yet been attempted in this framework. Note that Scapin et al. [20] have also presented a method for velocity extrapolation; nevertheless, integration only within an algebraic VOF solver was demonstrated in their work.

Our group is actively developing PSI-BOIL,¹ an in-house CFD solver with DNS capabilities. It has been verified and validated for a multitude of problems involving multiphase flows and interfacial mass transfer [19,21,22]. Although it includes a sharp-interface phase-change model, the phases have been represented using a smeared volume fraction (colour function) [23]. This approach carries with it several disadvantages, most prominently poor

¹ <https://github.com/PSI-NES-LSM-CFD/PSI-Boil>.

estimation of interfacial curvature, unphysical redistribution of mass during interfacial sharpening, and failure to capture the interface properly near fluid domain boundaries. Furthermore, special techniques for its coupling to species transport equation are required [22].

In order to overcome these issues, we have decided to implement the geometric VOF method into PSI-BOIL. We have already introduced the VOF method with geometric advection of Weymouth and Yue [24] and extended it from Cartesian to axisymmetric geometries [61]. In this paper, a coupling of this method for both grid configurations with the sharp-interface phase-change model of Sato and Niceno [19] and a modified version of the velocity extrapolation method of Malan et al. [17,18] are presented. Furthermore, species transport with implicit diffusion is considered using an algorithm adapted from our previous work [22]. Coupling of the geometric VOF method to species transport has been presented before in the open literature, most prominently in the work by Schlottke and Weigand [25] and subsequent works related to the DNS code FS3D [26]. Nevertheless, with their approach, the mass transfer rate is calculated from the concentration gradient, rendering their method incapable of simulating single-species problems. The species transport in FS3D is treated explicitly and special flux limiter functions are introduced to avoid concentration errors near the interface [27].

Our preliminary results for single-species simulations, including verification using 1D problems, have already been presented in Bures and Sato [28]. In this paper, the numerical approach is detailed and the results of one-dimensional verification benchmarks are repeated for completeness. Then, more advanced verification and validation exercise results are shown, both for 2D axisymmetric and 3D Cartesian grids. First-order accuracy of the method is demonstrated. Rising evaporating and condensing bubbles are simulated with reasonable agreement with experimental data; in the latter benchmark, non-condensable gases are included and the applicability of the method to problems without inherent symmetry and featuring turbulence is shown.

To the best of our knowledge, a multiphase geometric-VOF-based CFD solver demonstrating subgrid accuracy and consistently applicable to non-adiabatic problems with and without species transport has not yet been rigorously validated against non-trivial experimental benchmarks. As such, this work represents an important step in the development of multiphase codes capable of accurately resolving complex three-dimensional flows.

The outline of this paper is as follows: in Section 2, the numerical method is described; in Section 3, verification against analytical solutions and validation against experimental measurement are presented; finally, the conclusions are drawn in Section 4.

2. Numerical method

PSI-BOIL is a multiphase incompressible flow solver written in C++ and using Message Passing Interface (MPI) for parallelisation. The coupling of the geometric VOF method based on the algorithm described by Weymouth and Yue [24] with a phase-change model is presented in Section 2.1. In Section 2.2, the solution method for momentum conservation equations is summarised; finally in Sections 2.3 and 2.4, the details of the implementation of the energy conservation and species transport equations are described, respectively.

2.1. Interface tracking using a VOF algorithm accounting for phase change

In the VOF approach, the phases are represented in terms of a cell-wise phasic volume-fraction function, ϕ [1]. For a computational cell of volume V_c [m³], the volume fraction of Phase 1 (taken

here to be the liquid phase), ϕ_1 , is defined as:

$$\phi_1 = \frac{V_1}{V_c}, \quad (1)$$

where V_1 is the volume of the cell occupied by Phase 1. If only two phases are present (i.e. liquid and gas), $\phi_2 = 1 - \phi_1$; therefore, we drop the subscript 1 for brevity and refer to ϕ as the *liquid volume fraction*. The governing equation for ϕ for incompressible flow without phase change takes the form:

$$\frac{\partial \phi}{\partial t} + \nabla \cdot (\phi \vec{u}) = 0, \quad (2)$$

where \vec{u} is velocity [m/s]. A simple PLIC-VOF² algorithm to solve this equation in the time-discretised form, where superscripts indicate the time step and Δt is the time step length:

$$\frac{\phi^{n+1} - \phi^n}{\Delta t} = -\nabla \cdot (\phi^n \vec{u}), \quad (3)$$

coupled with momentum transport can be summarised in procedural steps as follows:

- Step 1. Reconstruct the interfacial geometry, calculating normal vectors and line/plane constants.
- Step 2. Advect the volume fraction field using directional splitting [29].
- Step 3. Calculate curvature and surface tension force.
- Step 4. Solve the momentum conservation equations to obtain a new velocity field.
- Step 5. Solve transport equations for other scalar fields (temperature, concentration, ...).
- Step 6. Advance the time step and go back to Step 1.

Several methods are available for normal vector calculations in Step 1; we use the ELVIRA algorithm of Pilliod and Puckett [30] for two-dimensional calculations and the Mixed Young-CC method of Aulisa et al. [31] for three-dimensional calculations. Interface reconstruction is performed using closed-form formulae without in-cell iterations. The height function method with a 3×7 stencil for 2D and a $3 \times 3 \times 7$ stencil for 3D problems utilising the local topology adaptation approach of Lopez [32] is used for curvature calculations.

In case of problems involving phase change, Eq. (2) becomes:

$$\frac{\partial \phi}{\partial t} + \nabla \cdot (\phi \vec{u}_l) = -\frac{s_m}{\rho_l}, \quad (4)$$

where s_m is the volumetric source due to mass transfer between phases [kg/m³s] [21]:

$$s_m = j_m \varphi_\gamma, \quad (5)$$

with j_m being the mass flux to the interface [kg/m²s] and φ_γ [m²/m³] the interfacial area density. The method to calculate j_m is given in Section 2.3.

Furthermore, \vec{u}_l in Eq. (4) is the liquid velocity. Note that the velocity field \vec{u} cannot be used here in the same way as in Eq. (2), because it is not divergence-free due to phase change. The volume fraction of the liquid ϕ must be advected by the liquid velocity \vec{u}_l . For a single time step, Eq. (4) can be split as follows (ϕ^* represents an intermediate value):

$$\frac{\phi^* - \phi^n}{\Delta t} = -\frac{s_m}{\rho_l}; \quad (6)$$

$$\frac{\phi^{n+1} - \phi^*}{\Delta t} = -\nabla \cdot (\phi^* \vec{u}_l). \quad (7)$$

A modified form of the above algorithm can be then proposed as:

² Piecewise linear interface calculating [4].

- Step 1. Calculate interfacial area density φ_γ needed for Eq. (5).
- Step 2. Calculate mass transfer s_m between phases using Eq. (5).
- Step 3. Calculate the intermediate volume fraction field using Eq. (6).
- Step 4. Reconstruct the interfacial geometry, calculating normal vectors and line/plane constants.
- Step 5. Calculate the liquid and gas velocity fields, \vec{u}_l and \vec{u}_g .
- Step 6. Advect the intermediate volume fraction field using directional splitting: Eq. (7).
- Step 7. Calculate curvature and surface tension force.
- Step 8. Solve the momentum conservation equations to obtain a new velocity field.
- Step 9. Solve transport equations for other scalar fields (temperature, concentration, ...).
- Step 10. Advance the time step and go back to Step 1

Step 1 and Step 5 are detailed below.

2.1.1. Interfacial area density calculation

To estimate the interfacial area density, several methods are available in the VOF framework [33]; however, in terms of accuracy and robustness, the Marching Cubes algorithm [34] is the superior approach, even when the $\phi = 0.5$ isosurface does not correspond to the phasic interface exactly, as discussed in Appendix A.

2.1.2. Liquid velocity calculation

In PSI-BOIL, single-field formulation is used to represent the momentum equations. Using this approach, only the single-fluid velocity \vec{u} can be calculated. A method to obtain the liquid velocity required for the correct solution of Eq. (7) was presented by Malan [17, pp. 64–66]. Using this method, values of \vec{u}_l in the interfacial cells and in the vapour phase are obtained using divergence-free extrapolation from the liquid phase, $\vec{u}_l = \vec{u} + \vec{u}^+$, where \vec{u}^+ is chosen such that:

$$\nabla \cdot \vec{u}^+ = -\nabla \cdot \vec{u}. \quad (8)$$

Eq. (8) can be satisfied by solving a Poisson problem for corrective pressure p^+ in direct analogy to the projection method of Chorin [35]. The resulting liquid velocity is evidently divergence-free. We have adopted this approach with the following minor changes:

1. We define the solution domain as illustrated in Fig. 1. The wall boundary is shifted by one layer further away from the interface in comparison with the original approach of Malan (cf. Fig. 1 and Fig. 11.2 of [17, p. 66]). This way, velocities at faces of cells containing the interface are always recalculated to avoid reliance on ITM-based information on face cutting (which is not sufficiently robust).
2. The density in the system matrix (Eq. 11.20 of [17, p. 66]) is taken to be the constant liquid density ρ_l . This accelerates the solution to the algorithm. The resulting Poisson problem has the form:

$$\nabla \cdot \left(\frac{\Delta t}{\rho_l} \nabla p^+ \right) = -\nabla \cdot \vec{u}. \quad (9)$$

Jacobi iterations [36] are used for solving Eq. (9). A flagging algorithm is used to label the interfacial and interface-adjacent cells: cells with a non-zero value of interfacial area density are marked as the former. The latter can be identified by having at least one neighbour cell whose centre lies in the other phase, i.e. satisfying the condition:

$$(\phi_{\text{cell}} - 0.5)(\phi_{\text{neighbour}} - 0.5) \leq 0. \quad (10)$$

Note that the same approach is used to obtain the divergence-free extrapolation of the gas velocity, \vec{u}_g , the only difference being the direction of the extrapolation.

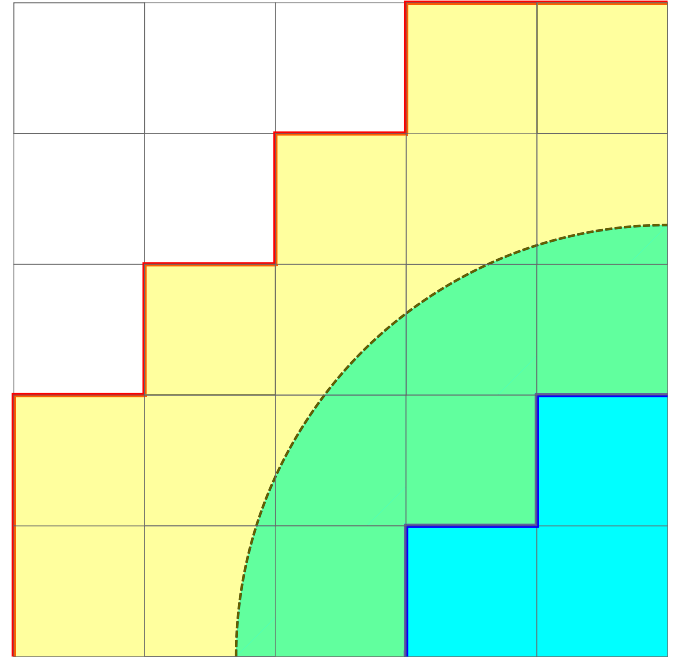


Fig. 1. Schematic representation of the velocity extrapolation domain; blue cells: liquid phase, white cells: gas phase, yellow shading: solution domain of the extrapolation Poisson problem, dashed line: phasic interface, orange line: free-flow boundary, blue line: wall boundary. (For interpretation of the references to colour in this figure legend, the reader is referred to the web version of this article.)

2.2. Momentum conservation

The momentum conservation is represented using the single-field Navier–Stokes equations [19]:

$$\frac{\partial(\rho \vec{u})}{\partial t} + \nabla \cdot (\rho \vec{u} \otimes \vec{u}) = -\nabla p + \nabla \cdot \left[\mu (\nabla \vec{u} + (\nabla \vec{u})^\top) \right] + \rho \vec{g} + \vec{f}_\sigma, \quad (11)$$

where p [Pa] is the pressure, \vec{g} [m/s²] the gravitational acceleration, \vec{f}_σ [N/m³] the surface tension force density and ρ [kg/m³] and μ [Pa s] the mixture density and dynamic viscosity, respectively. Assuming two phases, liquid and gas, the mixture density is calculated from its single-phase counterparts according to:

$$\rho = \phi \rho_l + (1 - \phi) \rho_g. \quad (12)$$

The mixture viscosity is calculated using the harmonic mixing rule:

$$\frac{1}{\mu} = \phi \frac{1}{\mu_l} + (1 - \phi) \frac{1}{\mu_g}. \quad (13)$$

The pressure p is obtained using the projection method of Chorin [35], which is used to satisfy the diabatic incompressibility condition:

$$\nabla \cdot \vec{u} = s_m \left(\frac{1}{\rho_v} - \frac{1}{\rho_l} \right). \quad (14)$$

Brackbill's Continuum Surface Force model [37] is used to estimate the surface tension force density, \vec{f}_σ .

The finite-volume formulation in the staggered-variable arrangement [38] is employed for the solution of the equations. For spatial discretisation, a second-order-accurate, central-difference scheme and a second-order flux-limiting, total-variation-diminishing (TVD) scheme [39] are used for the diffusion and advection terms, respectively. For time discretisation, backward and forward Euler methods are used for the diffusion and advection terms, respectively.

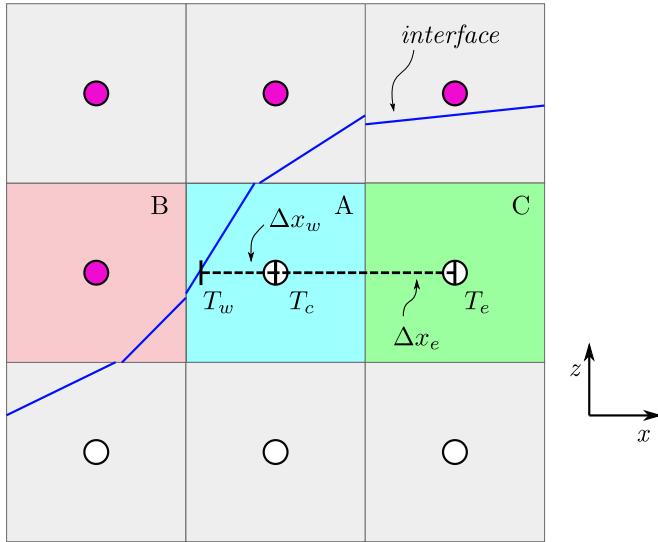


Fig. 2. Schematic representation of the discretisation of the energy conservation equation; cells with a white-centre: liquid phase (Eq. (15)), cells with a purple-centre: gas phase (Eq. (16)), blue line: phasic interface. The coloured cells are referred in the text. Only a two-dimensional domain is shown for simplicity. (For interpretation of the references to colour in this figure legend, the reader is referred to the web version of this article.)

2.3. Energy conservation

Energy conservation is solved using the two-fluid approach [19]:

$$C_{p,l} \left(\frac{\partial T}{\partial t} + \nabla \cdot (T \vec{u}_l) - T \nabla \cdot \vec{u}_l \right) = \nabla \cdot (\lambda_l \nabla T); \quad (15)$$

$$C_{p,g} \left(\frac{\partial T}{\partial t} + \nabla \cdot (T \vec{u}_g) - T \nabla \cdot \vec{u}_g \right) = \nabla \cdot (\lambda_g \nabla T), \quad (16)$$

with T being the temperature [K], C_p the volumetric heat capacity [J/m³K] and λ [W/mK] the thermal conductivity. A sharp-interface, finite-difference method is used for the spatial discretisation. Since the centre of each cell can be identified as either liquid or gas, Eqs. (15) and (16) can be solved simultaneously, taking into account the coupling through interfacial temperature T_γ , which can be either constant or variable (e.g. due to the presence of non-condensable gases [22]). The resulting decomposition of the computational domain is shown schematically in Fig. 2.

2.3.1. Diffusion term discretisation

The diffusion terms in Eqs. (15) and (16) are treated implicitly and the interfacial position is resolved with subgrid accuracy based on the PLIC-VOF reconstruction. As a result, the non-uniform spacing must be taken into account; we employ a three-point, central-difference scheme. Using the cyan-coloured cell **A** in Fig. 2 as an example, the x -component of the diffusion term in Cartesian geometry is calculated as (thermal conductivity assumed constant):

$$\lambda_l \frac{\partial^2 T}{\partial x^2} \approx \lambda_l \left[c_w T_w + c_e T_e - (c_w + c_e) T_c \right], \quad (17)$$

where T_w is the temperature in the “west” direction, i.e. the interfacial temperature T_γ , T_e the temperature in the “east” direction and T_c the temperature in the given cell. The coefficients c_w and c_e are deduced using a Taylor expansion as:

$$c_w = \frac{2}{\Delta x_w (\Delta x_w + \Delta x_e)}; \quad (18)$$

$$c_e = \frac{2}{\Delta x_e (\Delta x_w + \Delta x_e)}, \quad (19)$$

with Δx_w and Δx_e indicated in Fig. 2. In an axisymmetric geometry, a symmetric representation is used for the radial component:

$$\lambda_l \frac{1}{r} \frac{d}{dr} \left(r \frac{dT}{dr} \right) = \lambda_l \frac{1}{2} \left[\frac{d^2 T}{dr^2} + \frac{1}{r} \frac{d^2 (rT)}{dr^2} \right] \approx \lambda_l \left[c_w T_w + c_e T_e - (c_w + c_e) T_c \right], \quad (20)$$

where:

$$c_w = \frac{1}{\Delta x_w (\Delta x_w + \Delta x_e)} + \frac{1}{x_c} \frac{x_w}{\Delta x_w (\Delta x_w + \Delta x_e)} = \left(2 - \frac{\Delta x_w}{x_c} \right) \frac{1}{\Delta x_w (\Delta x_w + \Delta x_e)}; \quad (21)$$

$$c_e = \frac{1}{\Delta x_e (\Delta x_w + \Delta x_e)} + \frac{1}{x_c} \frac{x_e}{\Delta x_e (\Delta x_w + \Delta x_e)} = \left(2 + \frac{\Delta x_e}{x_c} \right) \frac{1}{\Delta x_e (\Delta x_w + \Delta x_e)}. \quad (22)$$

Here, x_c is the distance of the centre of the given cell from the axis of symmetry.

Note that for cells away from the interface, this discretisation scheme is second-order-accurate. At the interface, however, the asymmetry of the stencil results in first-order accuracy.

2.3.2. Advection term discretisation

The advection terms are treated explicitly. To evaluate the divergence of the “temperature flux” for phase i , $\vec{f}_i = T \vec{u}_i$, its values at the cell boundaries are calculated with a second-order TVD scheme. The ghost values of phasic velocities \vec{u}_l and \vec{u}_g needed for the discretisation in cells in the vicinity of the interface are obtained using the divergence-free extrapolation algorithm described above. The ghost temperature values are calculated by means of a linear extrapolation with the temperature of the interface T_γ and its position taken into account.

2.3.3. Phase-change model

The energy transport equation is coupled to the interface-tracking method by the phase-change model, since the mass flux to the interface j_m in Eq. (5) is calculated as [21]:

$$j_m = \frac{j_{q,l} + j_{q,g}}{L} = \frac{1}{L} \left(\lambda_l \nabla T \Big|_{l,\gamma} \cdot \vec{n} - \lambda_g \nabla T \Big|_{g,\gamma} \cdot \vec{n} \right), \quad (23)$$

where L is the specific latent heat of phase transition [J/kg], $j_{q,l}$ and $j_{q,g}$ the heat fluxes [W/m²] from the liquid and the gas sides to the interface, respectively, and \vec{n} the normal vector to the interface pointing towards the liquid. Furthermore, $\nabla T \Big|_{l,\gamma}$ and $\nabla T \Big|_{g,\gamma}$ are the temperature gradients at the liquid and gas sides of the interface [K/m], respectively. They are calculated using fourth-order-accurate upwind differences for non-uniform grids evaluated at the interface. The gradient components G_i which cannot be computed directly (such as both components of the liquid temperature gradient for the red-coloured cell **B** in Fig. 2) are obtained through extrapolation using the iterative solution of the Hamilton–Jacobi equation [40]:

$$\frac{\partial G_i}{\partial \tau} + \vec{n} \cdot \nabla G_i = 0, \quad (24)$$

where τ [m] is a pseudo-time variable (used only to advance to the steady-state solution). The values of G_i in cells away from the interface necessary to evaluate ∇G_i in Eq. (24) (such as the green-coloured cell **C** in Fig. 2) are calculated using fourth-order-accurate central differences.

2.4. Species transport in the gas phase

Transport of non-condensable species (NCG) in the gas is solved in the centre-of-volume reference frame [22]:

$$\frac{\partial[(1-\phi)\varepsilon]}{\partial t} + \nabla \cdot [(1-\phi)\varepsilon \vec{u}_v] = \nabla \cdot [(1-\phi)D\nabla \varepsilon], \quad (25)$$

where ε is the NCG volume fraction in the gas phase [-], \vec{u}_v the volume-averaged gas velocity and D the binary diffusion coefficient of the gas mixture [m^2/s]. The volume-averaged velocity is generally not equal to the mass-averaged one due to the unequal densities of the gas mixture components [22]; in this work, density of the gas phase is considered to be constant for simplicity. Then the velocities are equal and the volume fraction ε is equivalent to the mass fraction.

Eq. (25) is solved using the finite-volume formulation. Note that in Bureš and Sato [22], interface tracking was achieved by means of a smeared colour function [23] and a special solution framework for Eq. (25) had to be developed. In the current work, the volume fraction is used for interface tracking and the solution domain of Eq. (25) is determined by the condition $\phi < \phi_{\text{crit}}$, where the limiting factor ϕ_{crit} is chosen to avoid numerical errors in cells where $\phi \approx 1$. We have selected $\phi_{\text{crit}} = 0.999$ based on our previous experience – a sensitivity study for this parameter is shown in Section 3.4.

2.4.1. Diffusion term discretisation

The diffusion term is treated implicitly and a second-order-accurate, central-difference scheme is used for the spatial discretisation. The phasic interface is assumed to be impenetrable by the NCG. To calculate the cell-face area available for diffusion (i.e. the non-wetted fraction of the cell face represented by the product $(1-\phi)\Delta S$), the Marching Squares³ algorithm is used due to the robustness of this approach (as discussed in Appendix A).

2.4.2. Advection term discretisation

The advection term is treated explicitly. The volumetric flux at the cell boundaries $j_\varepsilon = (1-\phi)\varepsilon \vec{u}$ is calculated as [22]:

$$j_\varepsilon = \varepsilon_b(\vec{u} - j_\phi), \quad (26)$$

where j_ϕ is the liquid flux obtained from the VOF advection scheme. A second-order TVD scheme is employed to evaluate the boundary value of NCG volume fraction ε_b ; the ghost values of ε needed for the discretisation in the cells at the interface are calculated using an extrapolation in the normal direction across the phasic interface in the same manner as in Bureš and Sato [22], i.e. by solving Eq. (24) with G_i substituted by ε . Within this framework, the algorithm remains non-conservative with respect to the species concentration; the degree of non-conservation is discussed for one of the validation cases in Section 3.4.

2.4.3. Interfacial temperature

The dependence of the interfacial temperature T_γ on the NCG volume fraction ε_γ is modelled using the approximated Clausius-Clapeyron relation [41]:

$$T_\gamma^{\text{CC}} = T_0 / \left(1 - \frac{R_m T_0}{L} \ln(1 - \varepsilon_\gamma) \right). \quad (27)$$

Here, R_m [J/kg K] is the specific gas constant of the condensing species (liquid vapour) and T_0 the saturation temperature at given system pressure. Note that the accuracy of Eq. (27) depends on correct estimation of the latent heat L , since this quantity is generally dependent on interfacial temperature. If material-specific con-

stants are available, the Antoine-equation-based model for interfacial temperature [42] is also implemented:

$$T_\gamma^{\text{An}} = 273.15 + B / \left(\frac{B}{C + (T_0 - 273.15)} - \log_{10}(1 - \varepsilon_\gamma) \right) - C, \quad (28)$$

where B and C are Antoine equation coefficients. Under-relaxation of interfacial temperature is implemented as described in Bureš and Sato [22] and the under-relaxation factor is taken as 0.01.

3. Verification and validation

For verification of the method, the results of one-dimensional verification benchmarks from [28] are repeated for completeness; then, bubble growth in superheated quiescent liquid is simulated. For validation, problems of bubble growth in superheated liquid and condensation in subcooled liquid under the effects of gravity are considered. The latter benchmark involves non-condensable gases and thus it is also used for evaluating the degree of species non-conservation.

To evaluate mass conservation of the interface tracking method, evolution of the total volume of the confined gas phase V_g has been tracked. It is given as:

$$V_g(t) = \int_\Omega [1 - \phi(t)] dV' = V_\Omega - \int_\Omega \phi(t) dV' = V_\Omega - V_l(t). \quad (29)$$

Here, Ω represents the whole simulation domain and V_Ω is its total volume, which is a constant value; V_l is the time-dependent volume of the liquid phase. The total gas volume V_g has then been expressed using the volumetric phase-change rate \dot{V}_g [m^3/s] as:

$$\tilde{V}_g(t) = V_g(0) + \int_0^t \dot{V}_g(t') dt'. \quad (30)$$

Equivalence of the two above expressions, $V_g(t) = \tilde{V}_g(t)$, corresponds to the mass conservation condition for the interface tracking method. In all cases considered here, this has been achieved within numerical accuracy, that is, $V_g(t) - \tilde{V}_g(t) = \mathcal{O}(\epsilon)$, where $V_\Omega - [V_l(t) + V_g(t)] = \mathcal{O}(\epsilon)$.

3.1. One-dimensional problems

For verification purposes, we first consider the standard 1D evaporation problems in Cartesian configuration: the Stefan problem [7,43] and the sucking problem [7]. Fig. 3 shows the configuration common to both of these problems: a vapour film covering a wall with a temperature T_{wall} expands as a result of phase change occurring at the phasic interface, while the liquid bulk is pushed out through the outlet as a result of this expansion with the temperature at the outlet being T_{out} . The interfacial velocity u_γ is equal to:

$$u_\gamma = \frac{j_m}{\rho_v}, \quad (31)$$

Red: Stefan problem Blue: Sucking problem

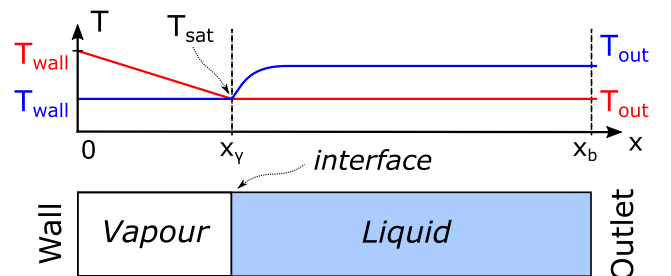


Fig. 3. Schematic representation of the one-dimensional phase-change problems.

³ Two-dimensional variant of the Marching Cubes algorithm [34].

Table 1
Physical properties of water at atmospheric pressure and saturation.

	Density ρ [kg/m ³]	Heat capacity c_p [J/kg K]	Thermal conductivity λ [W/mK]	Dyn. viscosity μ [Pa s]
Liquid	958.4	4216	0.679	2.80×10^{-4}
Vapour	0.597	2030	0.025	1.26×10^{-5}

Latent heat L [J/kg]: 2.258×10^6 , Surface tension σ [N/m]: 0.059, Saturation temperature T_{sat} [K]: 373.15.

and the liquid is uniformly advected with the Stefan velocity u_{stefan} :

$$u_{stefan} = j_m \left(\frac{1}{\rho_v} - \frac{1}{\rho_l} \right). \quad (32)$$

The analytical solution for the interfacial position as a function $x_\gamma(t)$ is given as [7,43]:

$$x_\gamma(t) = 2\beta_g \sqrt{\alpha_v t}, \quad (33)$$

where $\alpha_v = \lambda_v / (\rho_v c_{p,v})$ is the vapour thermal diffusivity [m²/s], $c_{p,v}$ being the vapour specific heat capacity [J/kg K], and β_g [–] a configuration-dependent growth constant. We consider a model problem representing a water system at atmospheric pressure, see Table 1 for physical properties.

In both problems, the heat is supplied from one side of the interface: in the Stefan problem, the wall at the origin is superheated ($T_{wall} > T_{sat}$) and heat diffuses to the phasic interface through the vapour film. Since the film is stagnant, the temperature profile is almost linear. In the sucking problem, the liquid bulk is superheated ($T_{out} > T_{sat}$). As a result, the sucking problem represents a combined advection-diffusion problem and a boundary layer forms in the vicinity of the phasic interface. Characteristics of both simulated problems are shown in Table 2. Here, t_0 corresponds to time chosen such that the position calculated using Eq. (33) corresponds to the initial film thickness $x_{\gamma,0}$. Furthermore, l_x is the extent of the considered simulation domain. Uniform grid discretisation with grid spacing Δx has been adopted. The number of computational cells for the coarsest grid considered is N_1 with the corresponding grid spacing being Δx_1 . A variable time step Δt is used with the limit imposed by the Courant number CFL :

$$CFL = \frac{u_{stefan} \Delta t}{\Delta x} < CFL_{max}, \quad (34)$$

and the CFL_{max} employed is listed in Table 2. The temperature profiles are initialised using the analytical solution [7,43].

Fig. 4 shows the calculated interfacial positions as functions of time for both problems. The grid level is defined in terms of the number of cells per domain extent l_x and normalised by the value for coarsest grid N_1 (see Table 2). To evaluate the accuracy order of the computational method, we use the relative error of the calculated growth constant, $\beta_{g,calc}$. The relative error E of a parameter A is calculated as:

$$E = \frac{A_{calculated}}{A_{theoretical}} - 1. \quad (35)$$

However, since the temperature field stretches during the simulation as the vapour film expands, the error of $\beta_{g,calc}$ evolves through time. For this reason, we consider the L^1 -mean value of the error

\bar{E}_1 , defined as:

$$\bar{E}_1 = \frac{1}{t_{max} - t_0} \sum_i |E_i| \Delta t_i = \frac{1}{t_{max} - t_0} \sum_i \left| \frac{\beta_{g,i}}{\beta_{g,theor}} - 1 \right| \Delta t_i, \quad (36)$$

instead. In Eq. (36), the sum is performed over all time steps, $(t_{max} - t_0)$ is the total simulation time, x_i the position of the interface at time step i and $x_{theor}(t_i)$ the position evaluated using the analytical solution. The third equality in Eq. (36) results from introducing the presumed evolution of the interfacial position, Eq. (33). For both problems, multiple levels of grid refinement have been calculated and Fig. 5 shows the L^1 -mean relative errors of the calculated growth constants β_g (Eq. (36)). Power law fits have been applied to the data in the asymptotic region and a method order of ~ 1 has been recovered for both problems. This is expected, since—as described in Section 2.3—the diffusion term of the energy transport equation is discretised with first-order accuracy near the interface and first-order extrapolation of temperature is used in the advection term. Improvements of the near-interface discretisation scheme will be attempted in future work.

3.2. Bubble growth in quiescent superheated liquid

Growth of a vapour bubble under zero gravity conditions in a uniformly superheated liquid is a standard verification benchmark for CFD codes (see e.g. [18,19,44]). An analytical solution to this problem was given by Scriven as [45]:

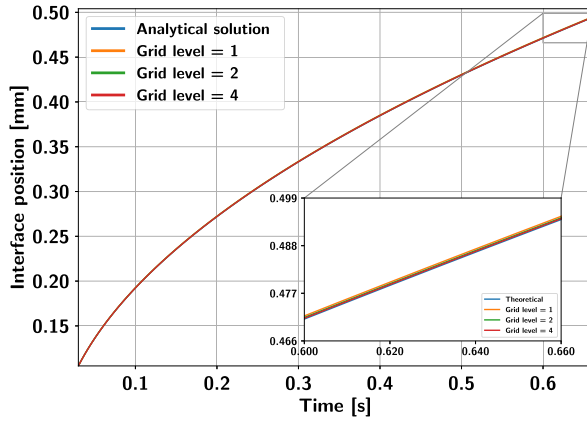
$$R(t) = 2\beta_g \sqrt{\alpha_l t}, \quad (37)$$

where R is the bubble radius, α_l is the liquid thermal diffusivity and β_g [–] is a configuration-dependent growth constant. We consider a model problem representing a water system at atmospheric pressure, see Table 1 for physical properties. With the choice of liquid superheat $\Delta T = T_{out} - T_{sat} = 1.25$ K, the growth constant β_g for this configuration is equal to 4.063. Bubble initial radius R_0 is taken as 50 μm .

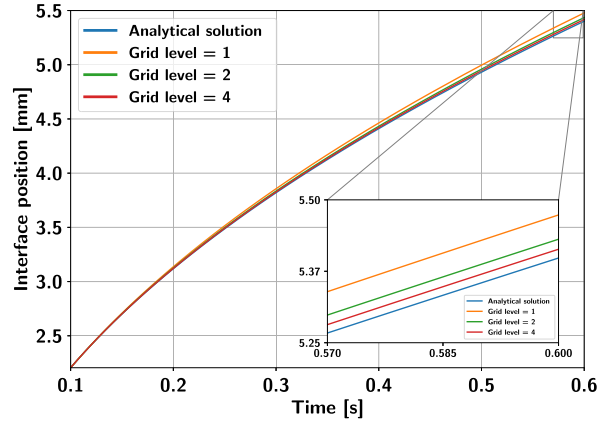
Both a two-dimensional axisymmetric and a three-dimensional Cartesian grid are considered. Using symmetry boundary conditions, only 1/2 and 1/8 of the bubble are simulated in these two cases, respectively. Domain side length S is taken as 187.5 μm in all directions. In the axisymmetric case, the bubble shape is initialised analytically; in the Cartesian case, stratified sampling is used to estimate the initial volume fraction field. The analytical solution [45] is used to initialise the temperature field. Fig. 6 shows a schematic representation of the domain used. The y-direction for the three-dimensional Cartesian case is not shown. At the outlet, the Dirichlet boundary condition for temperature is applied, $T = T_{out}$.

Table 2
Characteristics of the considered 1D evaporation problems. For the Stefan problem, $\Delta T = T_{wall} - T_{sat}$. For the sucking problem, $\Delta T = T_{out} - T_{sat}$.

	ΔT [K]	β_g [–]	t_0 [ms]	$x_{\gamma,0}$ [mm]	l_x [mm]	N_1 [–]	Δx_1 [μm]	CFL_{max} [–]
Stefan	10	0.0669	30	0.105	1	50	20	0.1
Sucking	5	0.7677	100	2.21	10	400	25	0.1



(a) Stefan problem.



(b) Sucking problem.

Fig. 4. Interfacial positions as functions of time for considered 1D evaporation problems and selected grid resolutions. The grid level is defined in terms of the number of cells per domain extent l_x and normalised by the value for the coarsest grid N_1 (see Table 2).

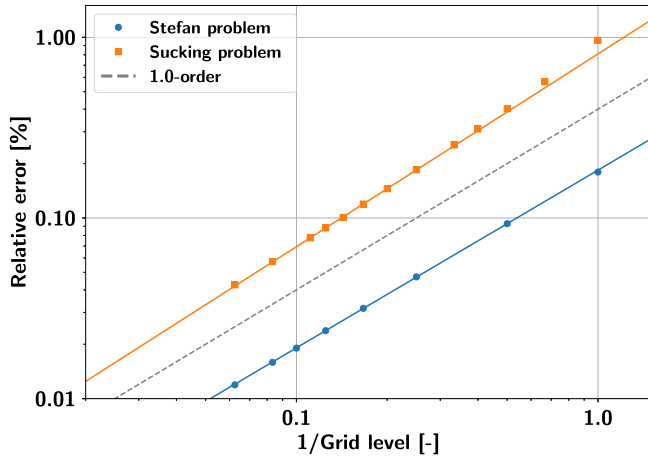


Fig. 5. L^1 -mean relative errors of the growth constant β_g (Eq. (36)) for the 1D evaporation problems as functions of inverse grid level (number of cells per domain extent l_x and normalised by the value for the coarsest grid N_1 , see Table 2). Solid lines correspond to power law fits of data points in the asymptotic region.

Uniform grid discretisation has been adopted. A variable time step Δt is used, with the limit imposed by the Courant number taken as:

$$CFL = \frac{u_{\max} \Delta t}{\Delta x} < 0.1, \quad (38)$$

where Δx is grid spacing and u_{\max} is the maximum velocity in the domain. A second upper limit is given by the capillary-wave condition [6,37]:

$$\Delta t < 0.10 \sqrt{\frac{(\rho_v + \rho_l) \Delta x^3}{\sigma}}. \quad (39)$$

The absolute minimum of these two criteria is the time step actually used in the simulation.

Fig. 7 shows the calculated bubble radii as functions of time for both axisymmetric and Cartesian cases and selected grid levels. The grid level is defined in terms of the number of cells per domain width S and normalised by 24 (value for coarsest grid). Evidently, very well converging behaviour has been achieved with both grids. Fig. 8 shows the L^1 -mean relative error (Eq. (36)) evaluated for bubble radius) of the calculated growth constant β_g with respect to the theoretical value. Power law fits have been applied to the data in the asymptotic region; the Cartesian results have

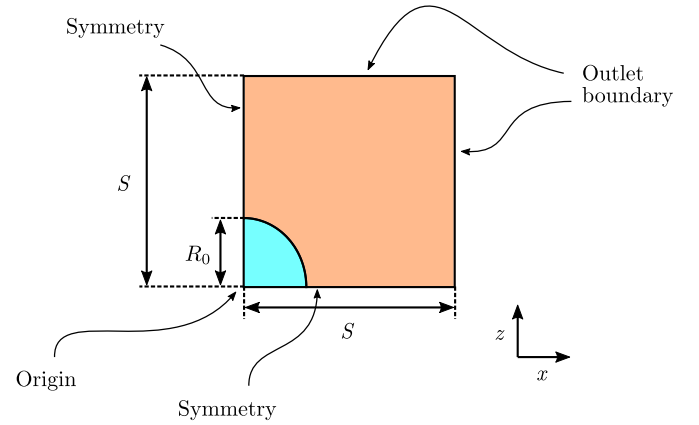


Fig. 6. Schematic representation of the domain used for the bubble growth in quiescent superheated liquid problem.

demonstrated a convergence order of ~ 1.5 , for the axisymmetric results, it is slightly higher. The smaller order of the Cartesian method could be attributed to the worse convergence characteristics of some aspects of the overall algorithm, e.g. normal vector and curvature calculations. Note that, for all grid levels, the time step in the simulation was limited solely by the capillary-wave condition, Eq. (39). As a result, the CFL number observed during the simulations scaled with the square root of the grid spacing, since:

$$CFL \propto \frac{\Delta t}{\Delta x} \propto \frac{\Delta x^{1.5}}{\Delta x} = \sqrt{\Delta x}. \quad (40)$$

This means the reduction of error with grid refinement must be partially attributed to the reduction of the time step. We assume a model for the error E of the form:

$$E \propto \Delta x^\alpha CFL^\beta \propto \Delta x^{\alpha+\beta/2}, \quad (41)$$

where α is the order of the method in space and β in time. Since first-order discretisation in time is used, $\beta = 1$, and we verify the first-order spatial accuracy already demonstrated in the previous section.

To illustrate the overall behaviour of the simulation, Fig. 9 shows instantaneous distributions of volume fraction, pressure, volumetric mass source, and temperature for one of the axisymmetric calculations. It can be observed that near-perfect levels of sharpness and symmetry have been achieved in the simulation.

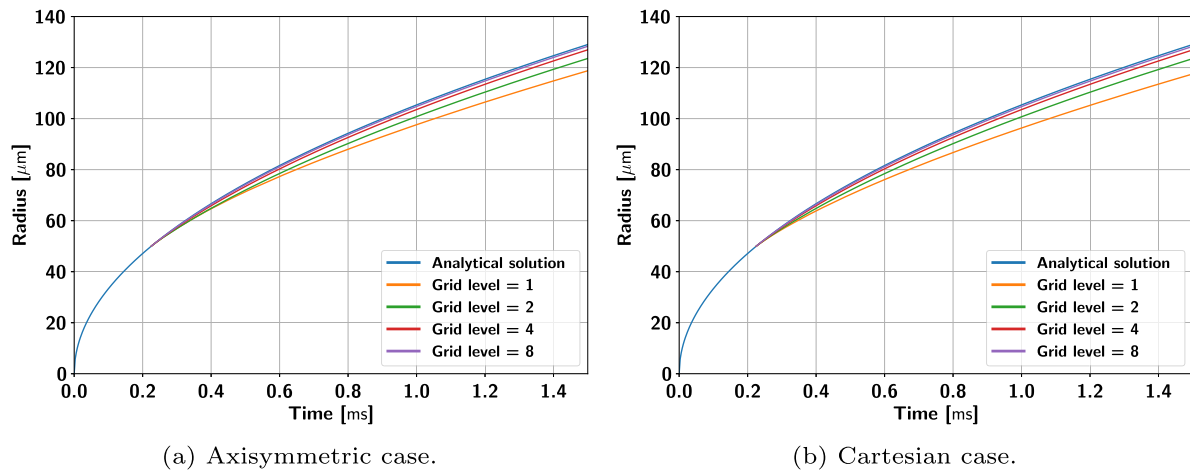


Fig. 7. Radius as a function of time for the bubble growth in quiescent superheated liquid problem. The grid level is defined in terms of the number of cells per domain width S and normalised by 24 (value for coarsest grid).

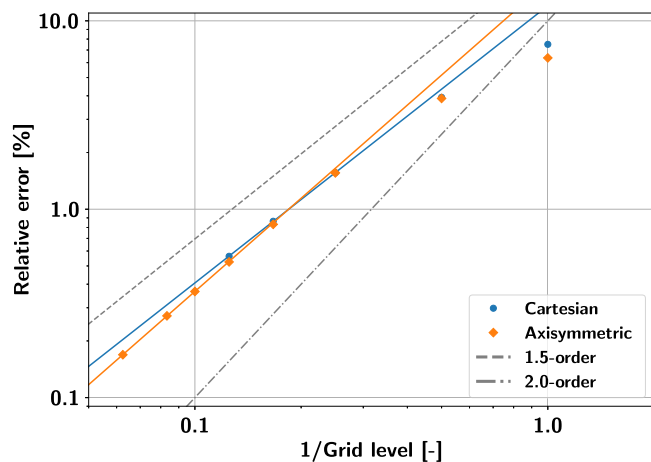


Fig. 8. L^1 -mean relative error (Eq. (36)) of the growth constant β_g for the bubble growth in quiescent superheated liquid problem as a function of inverse grid level (defined in terms of the number of cells per domain width S and normalised by 24). Solid lines correspond to power law fits.

Furthermore, Fig. 10 shows instantaneous distributions of volume fraction and temperature for one of the Cartesian calculations. In planes both normal to the coordinate axes and inclined with respect to the coordinate axes, near-perfect level of symmetry has been achieved.

3.3. Bubble growth in superheated liquid under gravity

The natural extension of the bubble growth benchmark is the inclusion of the gravity force. As a result, the bubble is no longer stationary, but rather rises through the liquid bulk due to buoyancy. The flow generated by the bubble motion increases heat transfer to the interface; subsequently, bubble growth rate is higher than the one predicted by the Scriven solution. Thus, both mass transfer at the interface and the overall bubble motion must be predicted accurately to obtain correct results. For validation, we have chosen the experimental data for ethanol of Florschuetz et al. [46]. Physical properties of an ethanol system at atmospheric pressure are listed in Table 3. The choice of ethanol rather than water is convenient from the numerical point of view: since thermal diffusivity of liquid ethanol at saturation is ~ 2.5 smaller than the one of liquid water, the temperature boundary layer around the rising bubble can be resolved with a lower number of computational

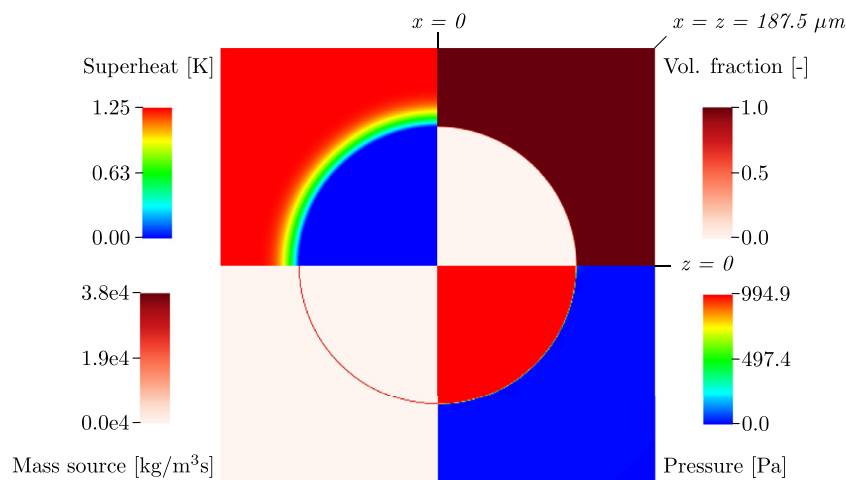


Fig. 9. Instantaneous distributions of volume fraction, pressure, volumetric mass source and temperature for the bubble growth in quiescent superheated liquid problem. Results are shown for grid level 8 (corresponding to 192 cells per domain width S) with axisymmetric configuration. Instantaneous radius is 120 μm , corresponding to a theoretical pressure jump due to surface tension equal to 983 Pa, pressure is zero at the outlet.

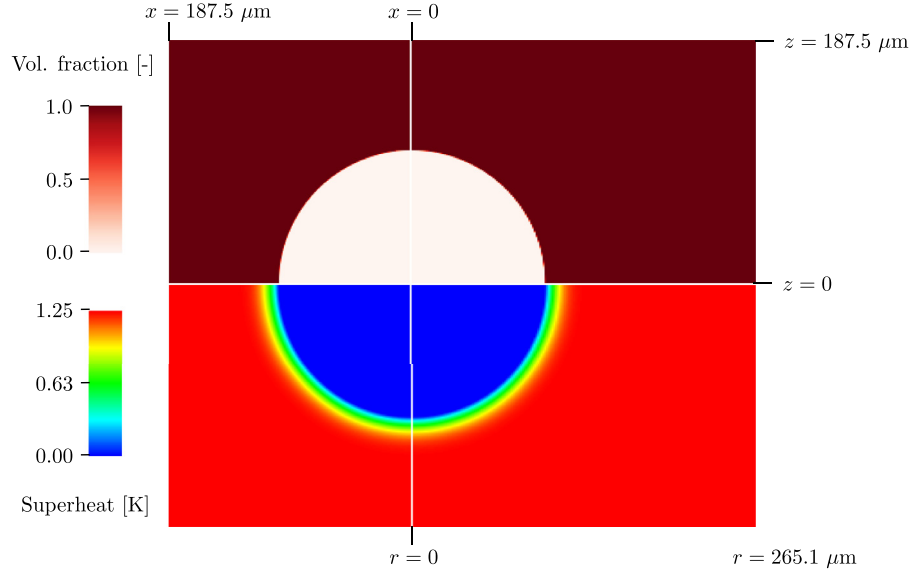


Fig. 10. Instantaneous distributions of volume fraction and temperature for the bubble growth in quiescent superheated liquid problem. Results are shown for grid level 8 (corresponding to 192 cells per domain width S) with Cartesian configuration. Left: cut in the $\theta = 0^\circ$ (x - z) plane. Right: cut in the $\theta = 45^\circ$ plane, the abscissa corresponds to the $r = \sqrt{x^2 + y^2}$ direction and ordinate to the z -direction.

Table 3
Physical properties of ethanol at atmospheric pressure.

	Density ρ [kg/m ³]	Heat capacity c_p [J/kg K]	Thermal conductivity λ [W/mK]	Dyn. viscosity μ [Pa s]
Liquid	757.0	3000	0.154	4.29×10^{-4}
Vapour	1.435	1830	0.020	1.04×10^{-5}

Latent heat L [J/kg]: 9.630×10^5 , Surface tension σ [N/m]: 0.018, Saturation temperature T_{sat} [K]: 351.45.

cells. For ethanol, experimental results for liquid superheat values 2.8–4.9 K have been reported in Florschuetz et al. [46]. In our calculations, we have chosen $\Delta T = T_{out} - T_{sat} = 3.1$ K. Note that for such configuration, the Scriven growth constant (Eq. (37)) is equal to 5.399. Bubble initial diameter D_0 is taken as 420 μm ; for this size, buoyancy effects are still negligible [46] and the zero-gravity analytical solution can be used to initialise the temperature distribution in the simulation. Gravitational acceleration g is set equal to 9.81 m/s^2 and acting in the negative z -direction.

Both a two-dimensional axisymmetric and a three-dimensional Cartesian grid are considered. Using symmetry boundary conditions for the three-dimensional grid, only 1/4 of the domain is simulated in this case. The height of the domain in the z -direction L_z is taken as 20 mm and the lateral width L_x (and L_y in the Cartesian case) as 4 mm. To reduce computational requirements of the simulation, lateral dimensions are discretised uniformly only in the centre of the column with stretched grid used for the rest. The bubble is initially positioned 1 mm above the column bottom. In the axisymmetric case, its shape is initialised analytically; in the Cartesian case, stratified sampling is used to estimate the initial volume fraction field. The zero-gravity analytical solution is used to initialise the temperature field. Fig. 11 shows a schematic representation of the domain after initialisation. The y -direction for the three-dimensional Cartesian case is not shown. Both at the outlet and at the no-slip walls, the Dirichlet boundary condition for temperature is applied, $T = T_{out}$.

For the axisymmetric configuration, four levels of grid refinement are simulated. For the Cartesian configuration, only the coarsest level is considered due to the prohibitive cost of such a simulation at higher grid levels. Table 4 summarises domain char-

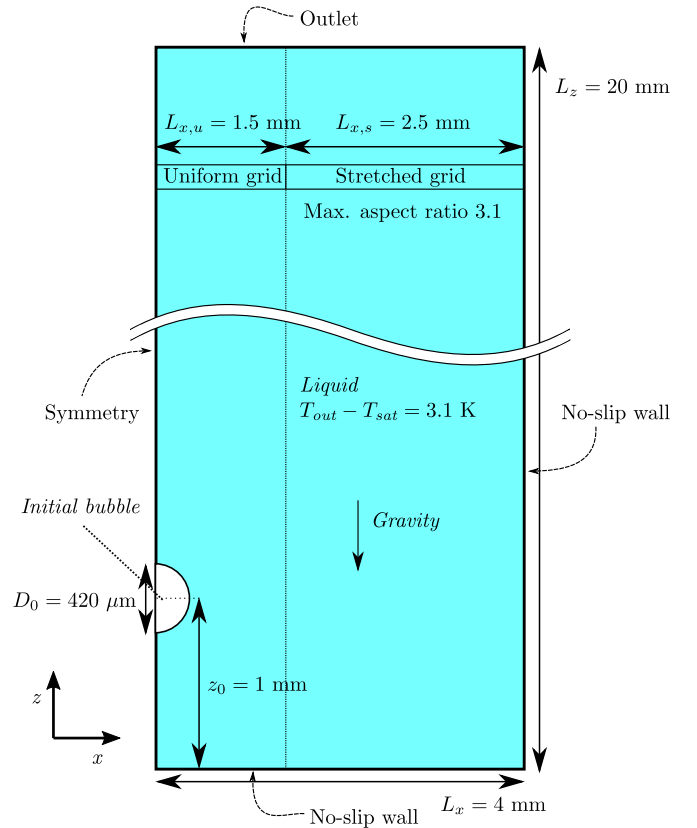


Fig. 11. Schematic representation of the domain used for the bubble growth under gravity benchmark.

acteristics of the simulated cases. A variable time step Δt is used, with the limit imposed by the Courant number taken as $CFL < 0.18$ and second upper limit given by:

$$\Delta t < 0.42 \sqrt{\frac{(\rho_v + \rho_l) \Delta x^3}{\sigma}}. \quad (42)$$

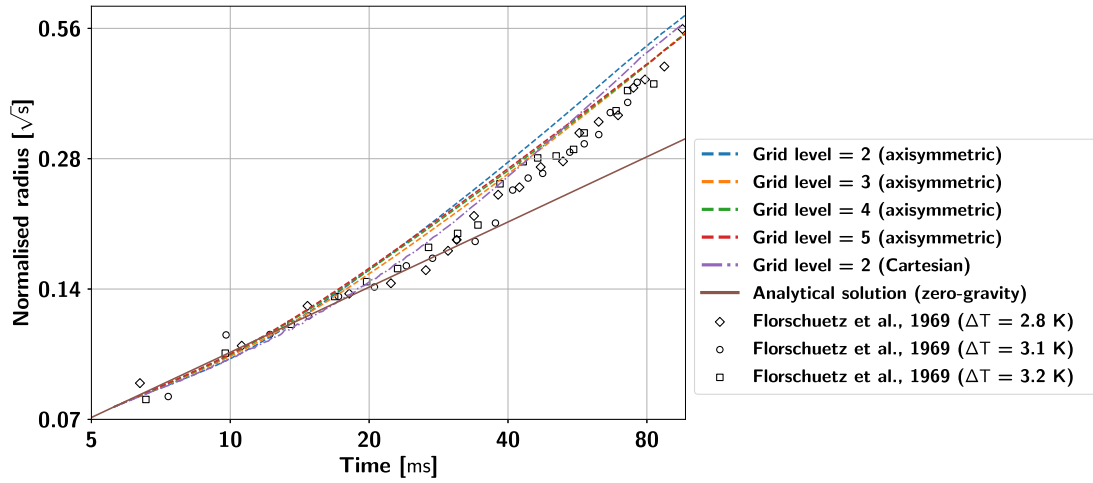


Fig. 12. Radius as a function of time for the bubble growth under gravity benchmark, compared with measurements [46] and theoretical predictions [45]. Results with both axisymmetric and Cartesian grids are shown. Grid level is defined in terms of the number of cells per domain width L_x and normalised by 21. Values on the ordinate are normalised by $2\beta_g\sqrt{\alpha_l}$.

Table 4

Domain characteristics of the bubble growth under gravity benchmark. Grid level is defined in terms of the number of cells per domain width L_x and normalised by 21.

	Grid level	Minimum grid spacing	Total number of cells
Axisymmetric	2	15.6 μm	215,040
	3	10.4 μm	483,840
	4	7.8 μm	860,160
	5	6.25 μm	1,344,000
Cartesian	2	15.6 μm	36,126,720

The absolute minimum of these two criteria is the time step actually used in the simulation.

Fig. 12 shows the calculated bubble radii as functions of time for all considered cases. Same expression as in Florschuetz et al. [46] is adopted to calculate the bubble radius R_{bub} :

$$R_{bub} = \frac{D_x + D_y + 2D_z}{8}, \quad (43)$$

where D_x , D_y , and D_z are bubble extents in the x -, y -, and z -directions, respectively. For axisymmetric simulations, $D_y = D_x$. To maintain consistency with the data representation used in Florschuetz et al. [46], normalisation by $2\beta_g\sqrt{\alpha_l}$ is used for R_{bub} (cf. Eq. (37)). It can be observed that good agreement with experimental data has been achieved. From the figure, it can be observed that axisymmetric simulation results—the coarsest simulation notwithstanding—vary only slightly with grid refinement; this is also evidenced by the plot of bubble Reynolds number Re_{bub} , calculated as (U_z being the bubble velocity in the z -direction):

$$Re_{bub} = \frac{\rho_l d_{bub} U_z}{\mu_l} = \frac{2\rho_l R_{bub} U_z}{\mu_l}, \quad (44)$$

shown in Fig. 13.

To illustrate the overall behaviour of the simulation, Fig. 14 shows instantaneous distributions of volume fraction, pressure, volumetric mass source, and temperature for one of the axisymmetric calculations. It can be observed that a near-perfect level of sharpness has been achieved in the simulation. The highest volumetric mass source is located on the bubble top, off-centre. Here the temperature boundary layer spans only 2–3 computational cells.

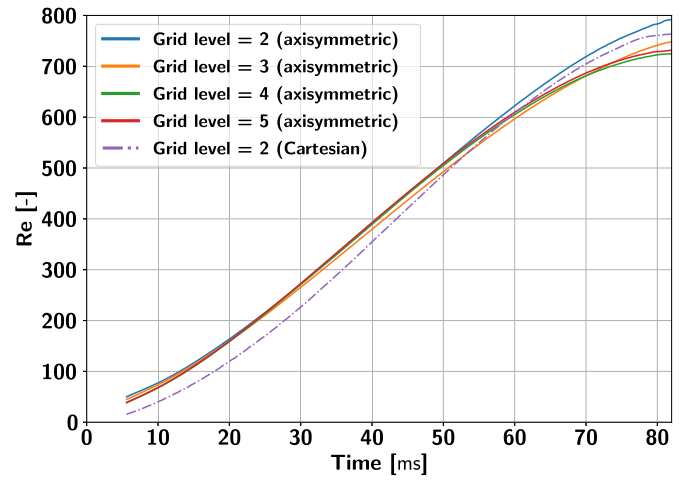


Fig. 13. Bubble Reynolds number as a function of time for the bubble growth under gravity benchmark. Results with both axisymmetric and Cartesian grids are shown. Grid level is defined in terms of the number of cells per domain width L_x and normalised by 21.

3.4. Bubble condensation with NCG in subcooled liquid under gravity

Direct-contact condensation of bubbles in subcooled liquid pools has been studied extensively in the past; nevertheless, only a limited number of works take into account the presence of non-condensable gases [47]. Our previous work focused on the demonstration of the capability of our numerical method to simulate this phenomenon [22]. In this paper, we validate our approach against an experimental data set. Note that in Bureš and Sato [22] smeared volume fraction (colour function) was used for phase representation, while the sharp volume fraction (VOF) is used in this paper.

In this type of experiment, a bubble is generated by injection of gas to a liquid pool through a nozzle. It detaches and starts to rise due to buoyancy. As a result of liquid subcooling, condensation occurs and the bubble shrinks continuously until an equilibrium volume V_∞ is achieved. Its value is dictated by the initial amount of NCG in the gas mixture and liquid subcooling $\Delta T = T_0 - T_{out}$ as:

$$V_\infty = V_{init} \frac{\varepsilon_{init}}{\varepsilon_\infty(\Delta T)}, \quad (45)$$

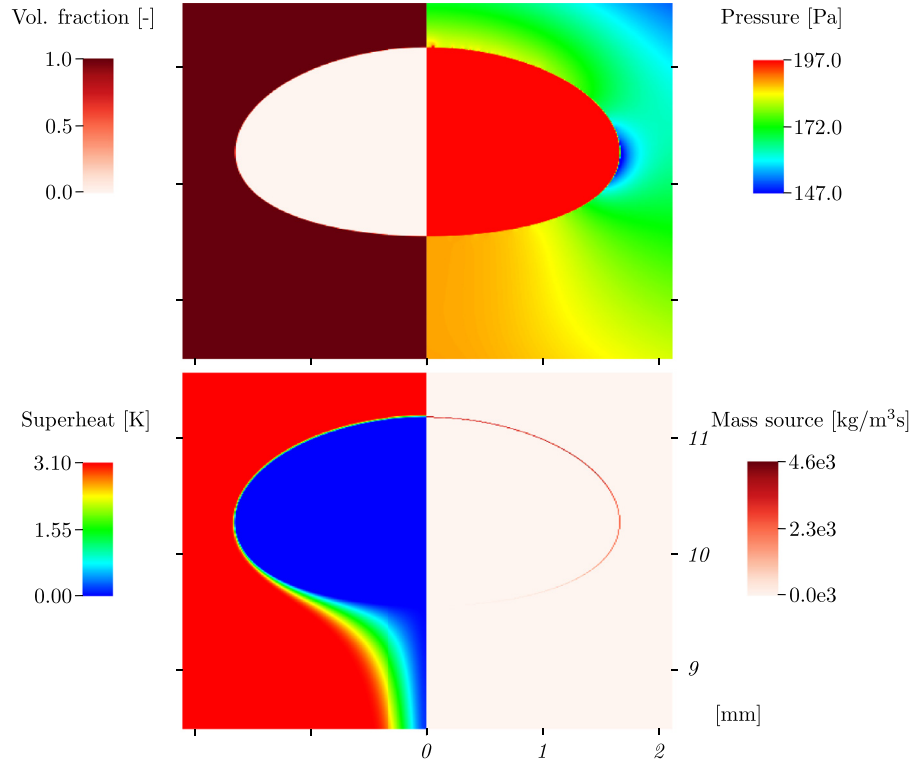


Fig. 14. Instantaneous distributions of volume fraction, pressure, volumetric mass source and temperature for the bubble growth under gravity benchmark. Results are shown for grid level 4 (corresponding to 84 cells per domain width L_x) with axisymmetric configuration. Radius calculated from Eq. (43) is 1.23 mm, corresponding to a theoretical pressure jump due to surface tension equal to 28.7 Pa, pressure is zero at the outlet.

Table 5

Selected experimental conditions [48] and simulation settings used for validation. The latter have been chosen by averaging the two experimental cases.

	System pres. p_0 [atm]	Liquid subcool. ΔT [K]	Initial bubble radius R_0 [mm]	Initial air vol. fraction ε_{init} [%]	Equilibrium air vol. fraction ε_∞ [%]
Exp. CFF2121	1	5.4	1.3	0.2051	16.84
Exp. CFF2221	1	5.4	1.5	0.1914	16.84
Simulation	1	5.4	1.4	0.1983	16.84

with T_0 being the reference saturation temperature at given system pressure, V_{init} the initial detached bubble volume, ε_{init} the initial NCG volume fraction, and ε_∞ the equilibrium NCG volume fraction. Its value is determined from the condition $T_\gamma(\varepsilon_\infty) = T_{out}$.

3.4.1. Simulation setup

As reference data, we have chosen the experiments of Kalman [48] involving condensation of refrigerant R-113⁴ bubbles with non-zero air content in a subcooled liquid refrigerant pool. This experiment has been compared to CFD results before, e.g. by Jia et al. [50]. Data sets of radius and height as functions of time for single bubbles are provided in Kalman [48] for several liquid subcooling values. In our calculations, we have chosen those for $\Delta T = 5.4$ K, Table 5 summarises the experimental conditions and values chosen for our simulation.

Physical properties of a R-113 system at atmospheric pressure are listed in Table 6. Majority of the values have been obtained from the NIST catalogue [49]. The latent heat value has been taken from [52]. The R-113/dry-air binary diffusion coefficient has been estimated using the FSG correlation [53,54] (presented here in SI units, except for diffusion volumes ς assumed in cm³ by

convention):

$$D_{FSG} = 10^{-7} \cdot \frac{101325}{p_0} \cdot \frac{T_0^{1.75}}{(\varsigma_v^{1/3} + \varsigma_n^{1/3})^2} \cdot \sqrt{\frac{10^{-3}}{M_v} + \frac{10^{-3}}{M_n}}. \quad (46)$$

The atmospheric pressure and the corresponding saturation temperature of R-113 are used as the reference pressure p_0 and temperature T_0 in Eq. (46). The molar masses M_v and M_n are equal to 187.4×10^{-3} kg/mol and 29.0×10^{-3} kg/mol, respectively. The diffusion volumes ς_v and ς_n have been taken in accordance with [53,54] as 138.9 cm³ and 19.7 cm³, respectively. For the dependence of the interfacial temperature T_γ on the NCG volume fraction ε_γ , we use the Antoine relation (Eq. (28)). The Antoine coefficients for R-113 have been taken from [51] and are presented in Table 7. Note that, for simplicity, we have assumed the material properties of NCG, i.e. density, viscosity, heat capacity and thermal conductivity, to be constant and equal to the R-113 vapour properties. As the air mass fraction remains $\lesssim 2.5\%$ throughout the experiment, we consider this simplification to be justified. Furthermore, since gas properties have negligible impact on the dynamics of bubble rise [55] and heat transfer occurs almost solely in the liquid, the main characteristics of the problem are well-captured.

During the bubble rise in this configuration, Reynolds numbers exceeding 1000 are observed. At those values, rectilinear motion and symmetric bubble oscillations are no longer guaranteed, as

⁴ 1,1,2-Trichloro-1,2,2-trifluoroethane [49].

Table 6
Physical properties of R-113 at atmospheric pressure.

	Density ρ [kg/m ³]	Heat capacity c_p [J/kg K]	Thermal conductivity λ [W/mK]	Dyn. viscosity μ [Pa s]
Liquid	1508	940.4	6.367×10^{-2}	4.904×10^{-5}
Vapour	7.424	691.4	9.506×10^{-3}	1.028×10^{-5}

Gas mixture diffusion coefficient D [m²/s]: 7.904×10^{-6} , Latent heat L [J/kg]: 1.467×10^5 , Surface tension σ [N/m]: 0.01470, Reference saturation temperature T_0 [K]: 320.735.

Table 7
Antoine-equation coefficients for R-113 [51].

A	B	C
6.88	1099.9	227.5

confirmed by the photographs presented in Kalman [48]. Bubbles in axisymmetric simulations exhibited strong non-physical oscillations often resulting in their splitting. Thus, reduced-size axisymmetric simulations were used only for evaluation of grid convergence during the initial, symmetric stage of the simulation and only results of full three-dimensional Cartesian simulations have been considered for detailed analysis. The height of the domain in the z -direction L_z is taken as 80 mm for the full simulations and 13.3 mm for the reduced-size ones. The lateral widths in the 3D Cartesian computations L_x and L_y are taken as 20 mm; for the axisymmetric simulations, the equivalent radial half-width $L_r = 10$ mm is used. To reduce computational requirements, lateral dimensions are discretised uniformly only in the centre of the column with stretched grid used for the rest. Gravitational acceleration g is set equal to 9.81 m/s^2 and acting in the negative z -direction.

In the experiment, the bubbles were generated by detachment from a vertical nozzle. We have successfully simulated such a setup

in Bureš and Sato [22]. In this work we want to precisely control the bubble initial radius and NCG content for quantitative comparison purposes. Thus, we omit the bubble-growth and detachment phases and instead initialise a stagnant spherical bubble 5 mm (2.5 mm for the axisymmetric simulations) above the bottom of the simulation domain using stratified sampling to estimate the initial volume fraction field. Temperature in the liquid is initialised as T_{out} . Initial value of the NCG volume fraction in the bubble is uniformly set equal to ε_{init} and its temperature is prescribed as $T_{init} = T_\gamma(\varepsilon_{init}) = 320.676 \text{ K}$ according to the Antoine relation. Fig. 15 shows a schematic representation of the full Cartesian domain after initialisation. The y -direction is not shown. Both at the outlet and at the no-slip walls, the Dirichlet boundary condition for temperature is applied, $T = T_{out}$, which is 5.4 K lower than the reference saturation temperature T_0 .

Multiple levels of grid refinement are simulated. Table 8 summarises domain characteristics of the simulated cases. A variable time step Δt is used, with the limit imposed by the Courant number taken as $CFL < 0.1$ and second upper limit given by:

$$\Delta t < 0.28 \sqrt{\frac{(\rho_g + \rho_l) \Delta x^3}{\sigma}}. \quad (47)$$

The absolute minimum of these two criteria is the time step actually used in the simulation.

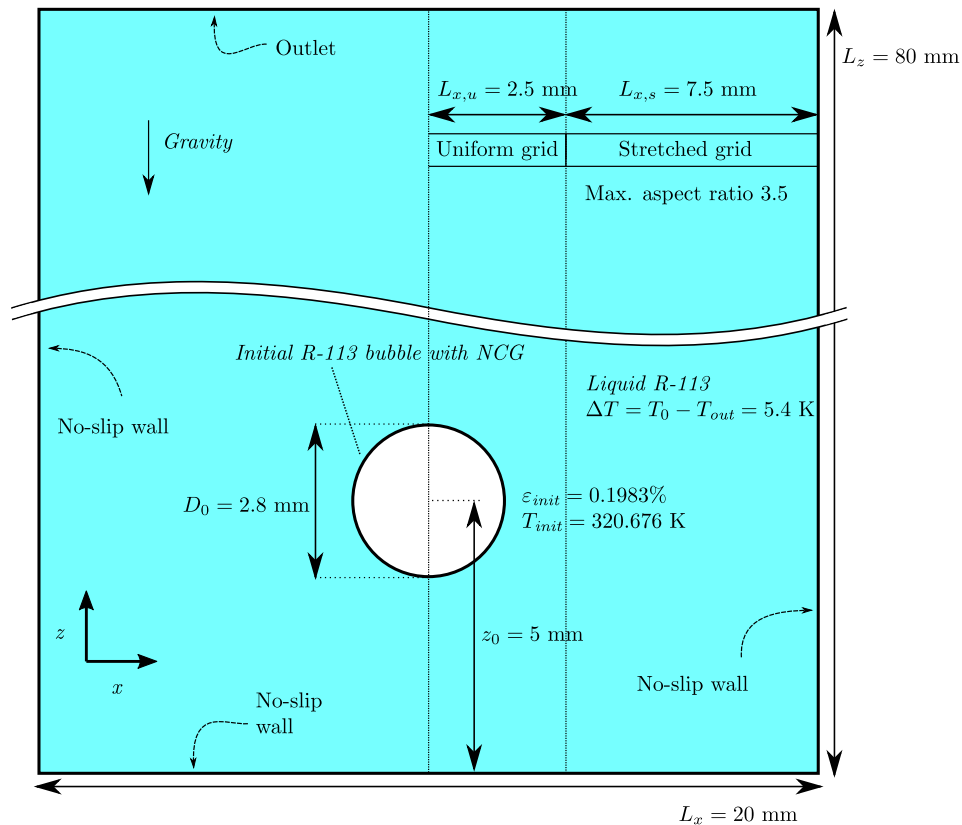


Fig. 15. Schematic representation of the domain used for the bubble condensation with NCG in subcooled liquid under gravity benchmark.

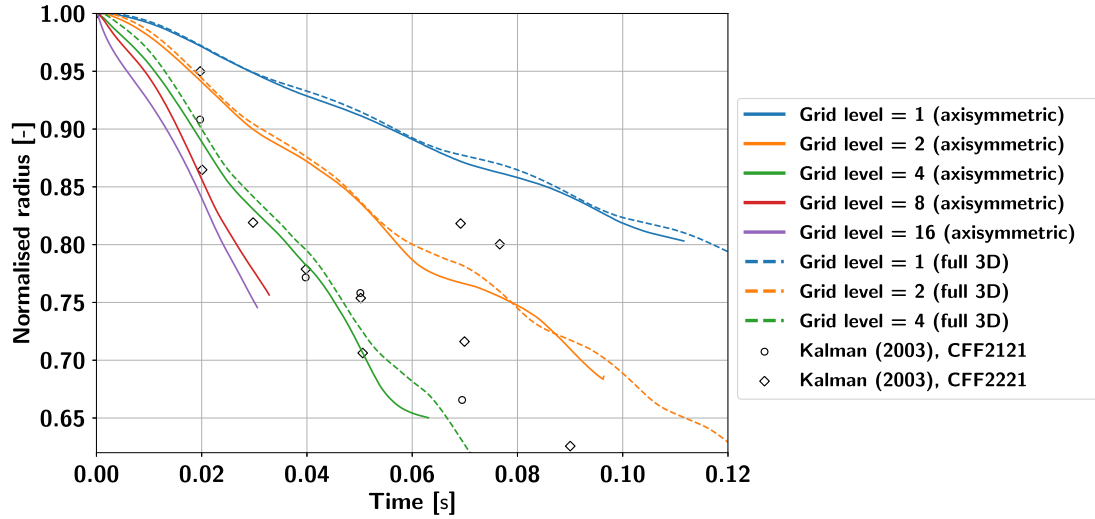


Fig. 16. Radius as a function of time for the bubble condensation with NCG in subcooled liquid under gravity benchmark, compared with measurements [48]; initial stage of the simulation is shown. Grid level is defined in terms of the number of cells per domain width L_x and normalised by 64 (value for the coarsest grid). Values on the ordinate are normalised by the initial bubble radius R_0 (see Table 5).

Table 8

Domain characteristics of the bubble condensation with NCG in subcooled liquid under gravity benchmark. Grid level is defined in number of cells per domain width L_x and normalised by 64 (value for the coarsest grid).

Grid level	Min. grid spacing	Number of cells (axisym.)	Number of cells (Cart.)
1	208.3 μm	3072	1,622,016
2	104.1 μm	12,288	12,976,128
3	69.44 μm	–	43,794,432
4	52.08 μm	49,152	100,663,296
8	26.04 μm	196,608	–
16	13.02 μm	786,432	–

3.4.2. Grid convergence study

Figs. 16 and 17 present the calculated volume-equivalent bubble radii and axial positions as functions of time, respectively, for all even levels of grid refinement during the initial, symmetric portion of the simulation. The axisymmetric simulations were terminated on the occurrence of unphysical bubble break-up. It can be seen that axisymmetric and Cartesian results are highly similar and a

converging behaviour has been achieved, even though rather high level of grid refinement (8+) is required to reach grid convergence. Due to the prohibitive cost of such grid refinement, these simulations could not have not been conducted in the full Cartesian geometry and the rest of the analysis presented here has been performed using the four calculated Cartesian results. In spite of the lack of full grid convergence, we believe that they bring useful insight into the dynamics of the problem.

3.4.3. Quantitative comparison with the experiment

Fig. 18 shows the calculated volume-equivalent bubble radii as functions of time for all considered levels of grid refinement in the full Cartesian representation. For grid level 1, the bubble becomes too small due to condensation with respect to the grid spacing (~ 5 grid cells per bubble volume-equivalent diameter at $t \gtrsim 0.35$ s) – the resulting under-resolution mars the rest of the simulation. Fig. 19 presents the calculated bubble axial positions as functions of time; the bubble rise velocity is evidently overestimated with respect to the experiment. Since the phase-change rate increases with the bubble Reynolds number (i.e. with its velocity), this could

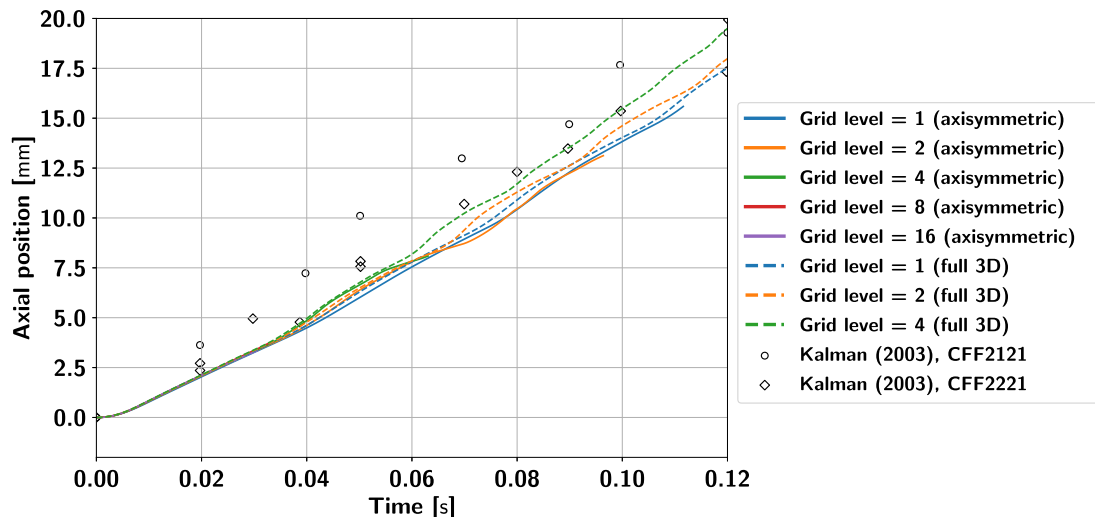


Fig. 17. Bubble axial position as a function of time for the bubble condensation with NCG in subcooled liquid under gravity benchmark, compared with measurements [48]; initial stage of the simulation is shown. Grid level is defined in terms of the number of cells per domain width L_x and normalised by 64 (value for the coarsest grid).

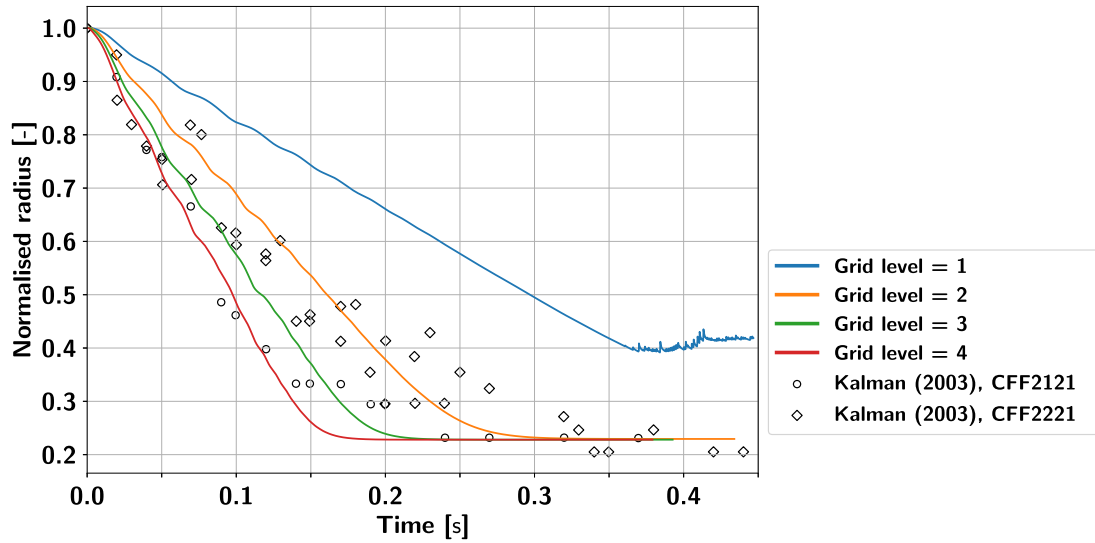


Fig. 18. Radius as a function of time for the bubble condensation with NCG in subcooled liquid under gravity benchmark, compared with measurements [48]. Grid level is defined in terms of the number of cells per domain width L_x and normalised by 64 (value for the coarsest grid). Values on the ordinate are normalised by the initial bubble radius R_0 (see Table 5).

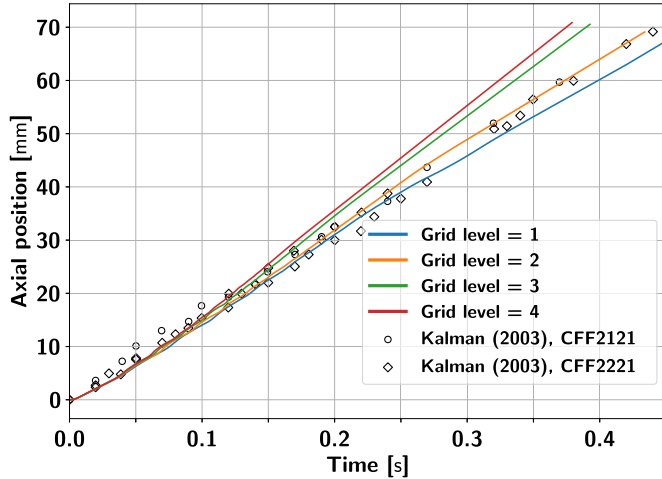


Fig. 19. Bubble axial position as a function of time for the bubble condensation with NCG in subcooled liquid under gravity benchmark, compared with measurements [48]. Grid level is defined in terms of the number of cells per domain width L_x and normalised by 64 (value for the coarsest grid).

explain the overestimation of the condensation rate by the simulation, observable in Figs. 16 and 18. The discrepancy between the experimental and computed rise velocities is clearly visible during the adiabatic stage of the problem after the equilibrium concentration is achieved. Although the overestimation of the rise velocity could be caused by the VOF advection scheme, the adiabatic simulations we have performed during our previous work have been able to capture the rise velocity correctly. Thus, the lower experimental bubble rise velocity could be instead attributed to the presence of surfactants in the liquid – in Kalman [48] as well as in the previous work with the same experimental apparatus [56], the presence of impurities in the liquid and the resulting immobilisation of the bubble surface during the condensation of immiscible fluids were assumed.

Fig. 20 shows additional computed results of this benchmark. In the plot of temporal evolution of the bubble Reynolds number (Fig. 20(a), calculated using Eq. (44)), the initial oscillations and their subsequent decay can be observed. At higher grid resolutions,

the terminal Reynolds number is achieved after the condensation process diminishes.

The NCG volume fraction (Fig. 20(b)) follows a sigmoidal curve. This could be explained as follows: at the beginning of the simulation, the value of ε_{bub} is low and the NCG have a negligible impact on the phase-change rate. Due to the rising motion, the superheated liquid surrounding the bubble is being constantly replenished, resulting in the volumetric flux \dot{V}'' [$\text{m}^3/\text{mm}^2\text{s}$] being approximately constant. And since:

$$4\pi R^2 \dot{V}'' = \dot{V} = 4\pi R^2 \frac{dR}{dt}, \quad (48)$$

the radius decreases linearly during this phase. This can be confirmed by observing the plot in Fig. 18. And since $\varepsilon_{bub} \propto R^{-3}$, the bubble NCG volume fraction initially follows a cubic relationship. As the bubble diminishes in size, the effect of NCG on the interfacial temperature increases and the phase-change rate decreases, ultimately reducing to zero. Note that by assuming a constant heat transfer coefficient in the liquid and linearising the Antoine relation, the approximate differential equation for the full bubble radius evolution could be obtained as:

$$\frac{dR}{dt} = -K(T_{init} - T_{out}) \frac{\varepsilon_{\infty} - \varepsilon(R)}{\varepsilon_{\infty} - \varepsilon_{init}} \approx -K\Delta T \left(1 - \frac{\varepsilon_{init}R_0^3}{\varepsilon_{\infty}R^3}\right), \quad (49)$$

where K is related to the liquid heat transfer coefficient h [$\text{W}/\text{m}^2\text{K}$] as:

$$K = \frac{h}{L\rho_v}. \quad (50)$$

A numerical solution of Eq. (49) can be used to fit the simulated evolution of the bubble radius, as shown in Fig. 21. The deduced values of the liquid heat transfer coefficients for all grid levels are presented in Table 9. They can be compared with the commonly-used correlations for h :

- The Ranz-Marshall correlation, originally developed for droplet evaporation [57]:

$$h_{RM} = \frac{\lambda_l}{d} \left(2 + 0.6Re^{0.5}Pr_l^{0.33}\right), \quad (51)$$

where d is the bubble diameter, Re the bubble Reynolds number and Pr_l the liquid Prandtl number:

$$Pr_l = \frac{\mu_l c_{p,l}}{\lambda_l}. \quad (52)$$

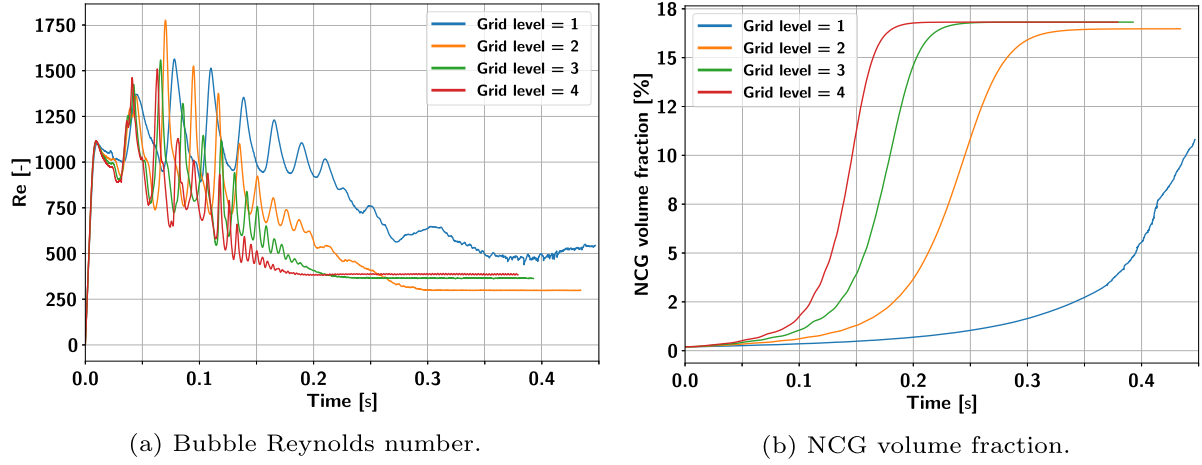


Fig. 20. Selected results of the bubble condensation with NCG in subcooled liquid under gravity benchmark. Grid level is defined in terms of the number of cells per domain width L_x and normalised by 64 (value for the coarsest grid).

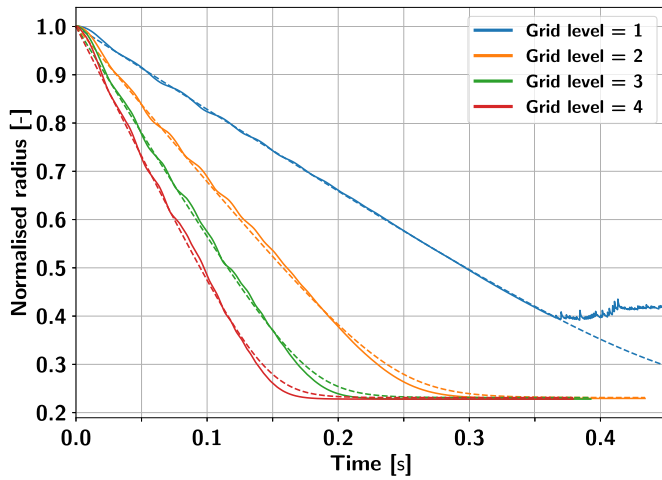


Fig. 21. Radius as a function of time for the bubble condensation with NCG in subcooled liquid under gravity benchmark, dashed lines represent the fitted numerical solutions of Eq. (49). Grid level is defined in terms of the number of cells per domain width L_x and normalised by 64 (value for the coarsest grid). Values on the ordinate are normalised by the initial bubble radius R_0 (see Table 5).

Table 9

Values of the liquid heat transfer coefficients h deduced using reduced-order modelling for the bubble condensation with NCG in subcooled liquid under gravity benchmark. Grid level is defined in number of cells per domain width L_x and normalised by 64 (value for the coarsest grid).

Grid level	h [W/m ² K]
1	493
2	929
3	1268
4	1548

For R-113, Pr_l is equal to 7.24.

- The Chen and Mayinger post-detachment correlation for bubble condensation [58]:

$$h_{CM} = \frac{\lambda_l}{d_{init}} \cdot 0.185 Re_{init}^{0.7} Pr_l^{0.5}, \quad (53)$$

where d_{init} is the bubble detachment diameter and Re_{init} the bubble detachment Reynolds number (i.e. d_{init} must be used as the length scale in Eq. (44)). For our calculations, we consider the initial bubble diameter as d_{init} .

To calculate the parameters needed for the expressions above (d and Re in Eq. (51) and Re_{init} in Eq. (53)), averaging during the non-equilibrium phase of the bubble condensation process has been used. The resulting mean value of the bubble Reynolds number is ~ 830 for grid levels 2, 3 and 4, i.e. slightly outside of the reported range of applicability of the Ranz-Marshall correlation ($Re < 800$) [59]. The Chen and Mayinger correlation is valid for $Re_{init} < 10^4$; in our simulations Re_{init} is about 1300. The resulting predictions from the correlations are essentially equal for grid levels 2, 3 and 4:

$$h_{RM} \approx 1400 \text{ W/m}^2 \text{ K}, \quad (54)$$

$$h_{CM} \approx 1700 \text{ W/m}^2 \text{ K}. \quad (55)$$

Although the values calculated using the reduced-order fitting (Table 9) approach the result of the Chen and Mayinger correlation, the axisymmetric results in the previous section indicate that, ultimately, the heat transfer coefficients deduced directly from our simulations will exceed those from the experimental correlation. A direct analysis of the data which formed the basis of the Chen and Mayinger correlation reveals that, for values of $Re_{init} \approx 1000$ (where, by coincidence, essentially all measured R-113 data is located), scatter of up to 100% has been reported. This suggests that our data is, overall, consistent with this experimental correlation.

3.4.4. Qualitative observations

To illustrate the overall behaviour of the simulation, Fig. 22 shows a detail of instantaneous distributions of temperature, NCG volume fraction, and pressure for one of the 3D Cartesian calculations at $t = 0.1$ s. At this point, the simulation still has a high level of axial symmetry, although a minor asymmetry can already be observed. The bubble oscillations can be clearly discerned from the temperature field and effects of vortex shedding can be identified in the temperature and pressure fields. The features of the volume-fraction distribution within the bubble, i.e. low concentration of NCG in the centre and on the top of the bubble and high concentration on its sides, are very similar to the ones observed in our previous work [22]. Fig. 23 shows the evolution of the simulated bubble motion from $t = 0.00$ s to $t = 0.34$ s by plotting the $\phi = 0.5$ isosurface. One snapshot per $\Delta t = 0.02$ s is shown from $t = 0.04$ s. The experimentally-observed overall dynamics as described by Kalman [48], i.e. strong initial deformation and oscillations and gradual transition to an oblate shape, are indeed observed in our simulation.

As the liquid in the bulk is stagnant overall, the effect of the bubble motion is localised and the introduced disturbances of the

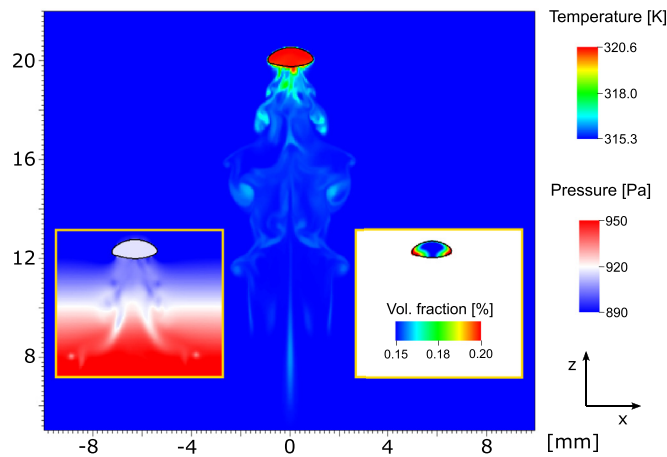


Fig. 22. Instantaneous distribution of temperature (main figure), NCG volume fraction (right inset), and pressure (left inset) for the bubble condensation with NCG in subcooled liquid under gravity benchmark at $t = 0.1$ s. Pressure is zero at the outlet. Results are shown for grid level 4 (corresponding to 256 cells per domain width L_x).

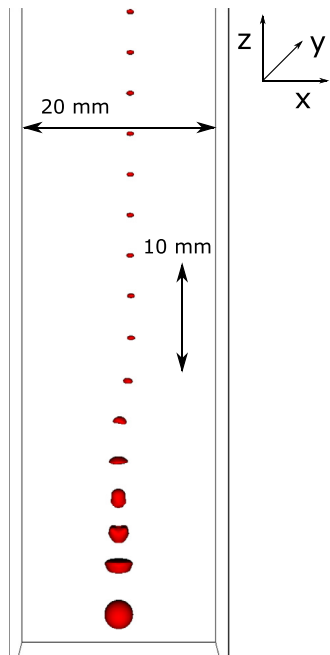


Fig. 23. Evolution of the rising bubble from $t = 0.00$ s to $t = 0.34$ s for the bubble condensation with NCG in subcooled liquid under gravity benchmark.

temperature field diminish slowly with respect to the time scales of the bubble rise; thus, they can be used to further examine the bubble motion. In Fig. 24, contours of disturbed temperature field at $t = 0.26$ s are shown. The equilibration of the bubble interfacial temperature with the liquid bulk temperature and the corresponding onset of adiabatic bubble rise are clearly visible between the two highest bubble contour snapshots. Furthermore, we can roughly distinguish four stages of the bubble motion:

- Initial stage ($t \lesssim 0.10$ s): rectilinear motion with oscillations.
- Transition stage ($0.10 \lesssim t \lesssim 0.13$ s).
- Zigzag motion stage ($0.13 \lesssim t \lesssim 0.20$ s).
- Terminal stage: rectilinear motion and gradual deceleration to terminal velocity ($0.20 \lesssim t$).

These stages are further illustrated by the plot of the transverse extents of the bubble in Fig. 25. The complexity of the bubble mo-

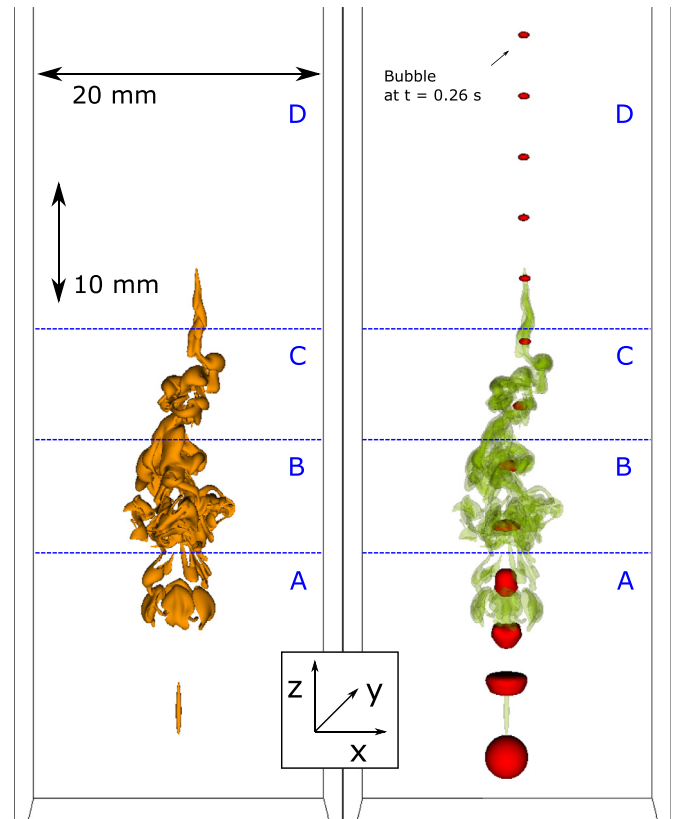


Fig. 24. Contours of disturbed temperature field at $t = 0.26$ s for the bubble condensation with NCG in subcooled liquid under gravity benchmark. In the figure on the right, it is overlaid by the evolution of the simulated bubble motion from $t = 0.00$ s to $t = 0.26$ s.

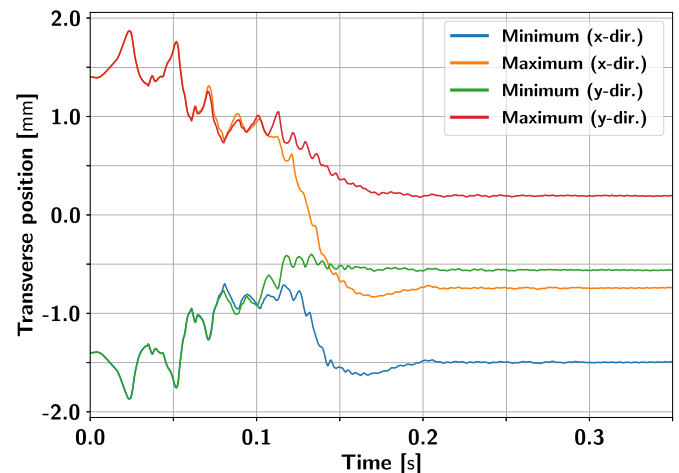
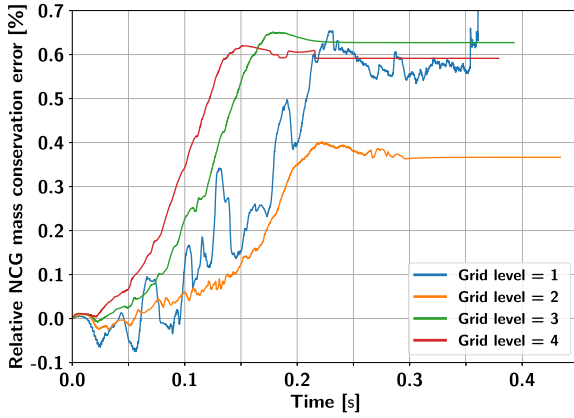
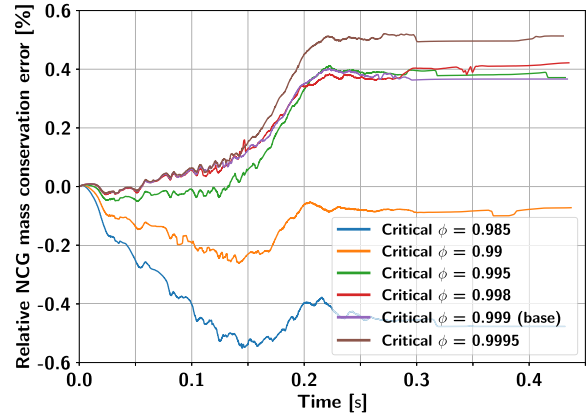


Fig. 25. Transverse (x and y) extents of the bubble as a function of time for the condensation with NCG in subcooled liquid under gravity benchmark. Results for the finest grid level are shown.

tion stems from the interplay of force balance, deformable bubble shape and non-constant volume of the bubble. It is rather interesting that the terminal rise velocity is achieved by deceleration due to the condensation reducing the bubble diameter. Particularly remarkable is the fact that we have managed to capture the zigzag motion stage, which is known to occur due to an instability resulting from an intimate coupling of bubble path and geometry [60], although only one turn is visible in the present simulation results due to the very fast condensation. While the transition from the linear motion to the zigzag motion has been often observed



(a) Effect of grid refinement.



(b) Sensitivity study for grid level 2.

Fig. 26. Species conservation error as a function of time (Eq. (56)) for the bubble condensation with NCG in subcooled liquid under gravity benchmark. Grid level is defined in terms of the number of cells per domain width L_x and normalised by 64 (value for the coarsest grid).

experimentally and numerically [60], the reverse transition is quite unusual – it requires the shrinkage of the bubble to occur, which in turn increases its sphericity. As bubble deformation is a prerequisite of the occurrence of the zigzag and/or helical motion [60], the linear motion is restored when the bubble becomes sufficiently spherical.

In Fig. 24, the structure of the vortices induced by the rising bubble is visualized by the temperature contour. For instance, in the region D where the bubble straightly raises, we can observe the double-threaded wake behind the bubble. In the region C, the wake and the vortices generated by the zigzag motion can be seen, the vortices featuring a kind of hairpin shape.

3.4.5. Evaluation of species conservation

As noted in Section 2, the species transport equation is non-conservative due to the extrapolation of ε across the interface and due to the limiting of the solution domain by the choice of a factor ϕ_{crit} . In this work, results with $\phi_{crit} = 0.999$ have been presented so far, a value chosen based on the experience gained from our preliminary simulations. Fig. 26(a) shows the evolution of the relative species conservation error, RCE, calculated as:

$$RCE = \frac{\Delta V_{NCG}}{V_{NCG,init}} = \frac{\sum_i^N \varepsilon_i (1 - \phi_i) \Delta V_i - \varepsilon_{init} V_{init}}{\varepsilon_{init} V_{init}}, \quad (56)$$

where N is the total number of grid cells. For an exactly species-conservative algorithm, RCE should be identically zero. It can be observed that at grid levels 3 and 4, the error of species-conservation is comparable at around 0.6% – at the end of the simulation, this corresponds to an absolute error of $\sim 0.006 \cdot 17\% \approx 0.1\%$.

To evaluate the effect of ϕ_{crit} on simulation results and its relation to the species conservation error, we have tested five additional values of ϕ_{crit} for grid level 2 in the Cartesian configuration: 0.985, 0.995, 0.998, 0.999, and 0.9995. Negligible impact on the tracked simulation parameters (bubble radius, Reynolds number, etc.) has been observed; this points at the overall robustness of the solution algorithm. Nevertheless, ϕ_{crit} strongly impacts the species conservation as can be observed from Fig. 26(b). It can be discerned that, starting from $t \approx 0.22$ s, the NCG volume remains essentially constant – this corresponds to the situation when the bubble does not deform and rises rectilinearly. Before that, two opposing effects play a role in the NCG non-conservation:

- **Bubble deformation:** as the bubble deforms, the extrapolation of ε across the interface gains on importance. Since constant extrapolation is used, when the ε gradient points towards the in-

terface (see Fig. 22), NCG mass is lost due to this effect. The lower the ϕ_{crit} , the more significant this phenomenon is.

- **Generation of flotsam:** due to the errors in the VOF advection, liquid cells with $\phi \lesssim 1$ (flotsam) are generated during the bubble rise. If the ϕ_{crit} is set too high, the solution domain of the NCG transport equation will contain erroneous cells, which can affect the NCG conservation.

As can be seen from Fig. 26(b), for low ϕ_{crit} values, the initial bubble oscillation phase results in a significant loss of NCG mass due to extrapolation. After the oscillations diminish, the flotsam errors start to dominate with their effect gaining on importance with increasing ϕ_{crit} . Due to these two sources of error having opposite trends, the optimal choice of ϕ_{crit} depends on the given problem. On the other hand, we can conclude that the non-conservation error is only weakly sensitive to ϕ_{crit} for values close to the baseline (0.995–0.999), which confirms it as a good initial choice.

While the results of this validation exercise are encouraging, the lack of species conservation and the accuracy limited by grid spacing points at the need of further development of the species transport solver. Achieving inherent species conservation and sub-grid accuracy akin to the rest of the computational method will be attempted in future work. Additionally, further development effort (e.g. higher-order discretisation, adaptive grid refinement) is necessary to successfully demonstrate grid convergence in the Cartesian geometry.

4. Conclusions

In this work, a numerical method for the direct numerical simulation of phase change using a sharp-interface algorithm coupled to the diabatic geometric VOF method has been described. Transport of NCG in the gas phase as well as their effect on the interfacial heat and mass transfer processes are accounted for using a phase-change model consistently applicable to single-species and multi-species problems. Particular emphasis has been placed on the estimation of the interfacial area density needed for the calculation of the mass-transfer rate; the Marching Cubes algorithm has been found to be the best-performing method.

A number of benchmark simulations have been performed to test the numerical algorithm. Aside of standard 1D evaporation problems, bubble growth in superheated quiescent liquid has been simulated using 2D axisymmetric and 3D Cartesian representations. Near-perfect levels of sharpness and symmetry have been achieved and first-order accuracy has been demonstrated. To validate the algorithm described in this paper, rising evaporating and

condensing bubbles have been simulated with reasonable agreement with experimental data, discrepancies being attributed to the presence of impurities in the experiment. In the latter benchmark, applicability of the method to problems without inherent symmetry and featuring turbulence and NCG transport has been shown. Furthermore, the heat transfer coefficient has been evaluated using a reduced-order model and found to be consistent with the experimental correlations and the observed transitions of the bubble rise motion from rectilinear to zigzag and back to rectilinear have been described. Finally, the degree of species-conservation error has been discussed and its impact has been found to be minor.

To the best of our knowledge, this work represents the first successful application of a diabatic geometric VOF method coupled with a sharp-interface phase-change model and species transport to non-trivial problems and the performance of our algorithm in the verification and validation exercise represents an important step in the development of codes capable of accurately resolving complex three-dimensional multiphase flows.

In future work, the algorithm will be thoroughly validated for wall-bounded multiphase flows including conjugate heat transfer, such as nucleate boiling. Furthermore, we will continue developing our simulation method with the main aim to (i) improve the overall accuracy of the method and (ii) achieve of inherent species conservation and subgrid accuracy of the species transport solver.

Declaration of Competing Interest

The authors declare that they have no known competing financial interests or personal relationships that could have appeared to influence the work reported in this paper.

CRediT authorship contribution statement

Lubomír Bureš: Conceptualization, Methodology, Software, Validation, Writing - original draft, Visualization. **Yohei Sato:** Conceptualization, Writing - review & editing, Supervision, Funding acquisition, Project administration.

Acknowledgements

This work is supported by the [Swiss National Science Foundation](#) (SNSF) under grant no. [200021_175893](#).

Appendix A. Interfacial area density calculation

In the context of VOF methods, the $||\nabla\phi||$ function or its scaled variants are commonly used to estimate the interfacial area density [33]. These methods, based on simple calculations of gradients, could be termed *algebraic methods*. Conversely, the interfacial area of a PLIC surface in a computational cell can be calculated as a by-product of the geometric reconstruction algorithm. Such a method could be thus termed *geometric* and an example of its implementation can be found e.g. in Soh et al. [33].

For interface-tracking methods (ITM), where the phasic interface is associated with a certain isosurface, such as the zero level for the Level Set ITM [5], interface reconstruction bears similarity to the rendering process in computer graphics and the Marching Cubes (MC) algorithm [34] can be used. While the VOF-based phasic interface cannot be strictly identified with the $\phi = 0.5$ isosurface, only a minor difference is expected between these two, which should be weighed against the robustness and sharpness of the MC algorithm.

We consider the volume fraction ϕ to be defined at cell centres of a Cartesian grid. For assessment of interfacial area density calculations, we consider three algebraic methods, for which φ_γ is

given as [33]:

$$\varphi_{\gamma,A} = ||\nabla\phi||; \quad (\text{A.1})$$

$$\varphi_{\gamma,B} = 2\phi||\nabla\phi||; \quad (\text{A.2})$$

$$\varphi_{\gamma,C} = 6\phi(1-\phi)||\nabla\phi||. \quad (\text{A.3})$$

The two scaled approaches, $\varphi_{\gamma,B}$ and $\varphi_{\gamma,C}$, have been developed to reduce the smearing of the interface. The disadvantage of approach B lies in its lack of symmetry, while approach C is known to strongly underestimate the interfacial area [33]. For the gradient calculation, we use the node-averaged values of ϕ ; the exact choice of the discretisation of $\nabla\phi$ does not significantly affect the results. For further comparison, we consider the geometric approach based on identifying the intersections of the PLIC-plane with the cell edges, similar to the one described in Soh et al. [33]. In order to avoid spurious interfaces created due to errors in volume fraction advection, we consider only cells in the vicinity of the interface. These cells can be identified by using Eq. (10). Finally, we also consider the interfacial area density calculated using the Marching Cubes algorithm based on node-averaged values of ϕ for comparison.

As a first test case, we analytically initialise a 2D circle centred in a periodic domain. We take its diameter as $D = 1.01N\Delta x$, where Δx is the grid spacing and N is a grid level quantifying the degree of grid refinement (approximately the number of cells per circle diameter). Uniformly discretised square is used as the computational grid. Fig. A.27 shows the calculated relative error (Eq. (35)) of total interfacial area as a function of $16/N$. The results for algebraic approach C are not shown as the underestimation of $\varphi_{\gamma,C}$ is about 50% for all levels of grid refinement. It can be seen that the other algebraic methods feature an asymptotic bias of about 0.2%, while the asymptotic bias of the MC method is $\sim 0.01\%$. The MC method is clearly best-performing overall.

In terms of identifying interfacial cells, the algebraic approach C, the geometric approach and the MC method all exhibited zero error. Note that this is not guaranteed for the Marching Cubes algorithm; in other configurations it can over/underestimate the total number of interfacial cells due to the misalignment of the VOF interface with the $\phi = 0.5$ isosurface. The algebraic approach A distributes the interfacial area over a band of cells near the interface, resulting in an overestimation of the total number of interfacial cells by a factor of 3 at all levels of grid refinement. For the algebraic approach B, the overestimation factor asymptotically approaches 2.

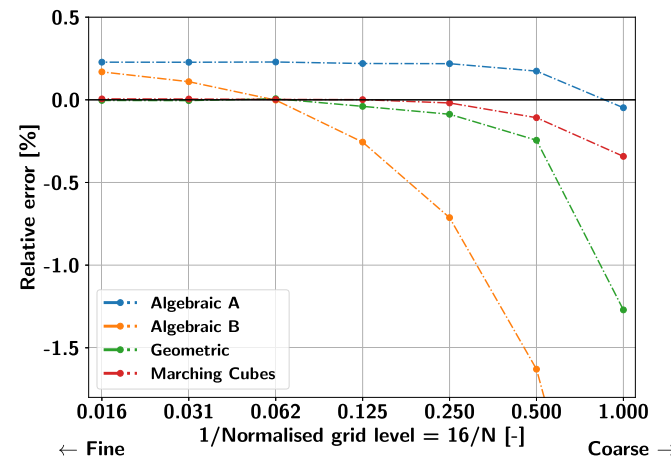


Fig. A27. Relative error of total interfacial area for a 2D circle as a function of the reciprocal of grid resolution. Base-2 logarithmic abscissa is used.

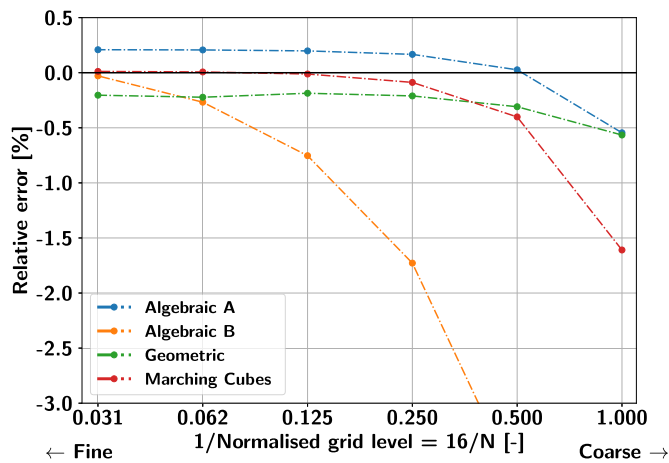


Fig. A28. Relative error of total interfacial area for a 3D sphere as a function of the reciprocal of grid resolution. Base-2 logarithmic abscissa is used.

As a second test case, we extend this problem to three dimensions. Since it is impossible to initialise the volume fraction distribution corresponding to a sphere on a Cartesian grid analytically, we use stratified sampling with $m = 20^3 = 8000$ evaluations per cell to initialise the sphere, i.e. a cell near the interface is divided into $20 \times 20 \times 20$ subcells and we evaluate if their centres are located inside or outside of the sphere. Fig. A.28 shows that the results for algebraic approaches and the MC method are very similar to the two-dimensional case (results for algebraic approach C are again omitted). Conversely, the results of the geometric method deteriorate significantly; we can observe that it features a non-zero bias ($\sim -0.2\%$), which is a result of the non-exact initialisation of the sphere. By increasing the number of stratified sampling points m , the magnitude of the bias decreases. Since the other methods are essentially insensitive to the value of m , this shows the lack of robustness of the geometric method. The MC method is again clearly best-performing.

For this problem, the Marching Cubes algorithm misestimates the total number of interfacial cells by up to several percent, depending on the grid resolution and the number of points m . Results for other approaches remain similar to the two-dimensional case.

Based on these two test cases and the requirements laid out in Section 1, it is evident that for sharp-interface VOF method with phase change, only the geometric approach and MC method are possible candidates for interfacial area estimation with the superior performance of the MC method stemming from its overall robustness. In spite of the error of area computed by the algebraic approaches A and B being minor, they are not considered due to the smearing of the interfacial area density. To complement the presented static analysis, Fig. A.29 shows the evolution of the relative error of total interfacial area for a 2D circle with $N = 128$ advected in the diagonal direction. The circle is advected over a distance equal to $2\sqrt{2}D$ with $CFL = 0.05$. Both for the geometric approach and the MC method the interfacial area slowly increases over time due to the deformation of the circle caused by errors in the advection scheme, even though the total volume of both phases is kept exactly constant in time. While both approaches started with an error of total area ≈ 0 , the spurious increase for the geometric approach is faster and significantly more erratic. This confirms the superiority of the MC method even when the VOF interface does not perfectly align with the $\phi = 0.5$ isosurface. Similar conclusions can be reached when the advection of a 3D sphere is tested.

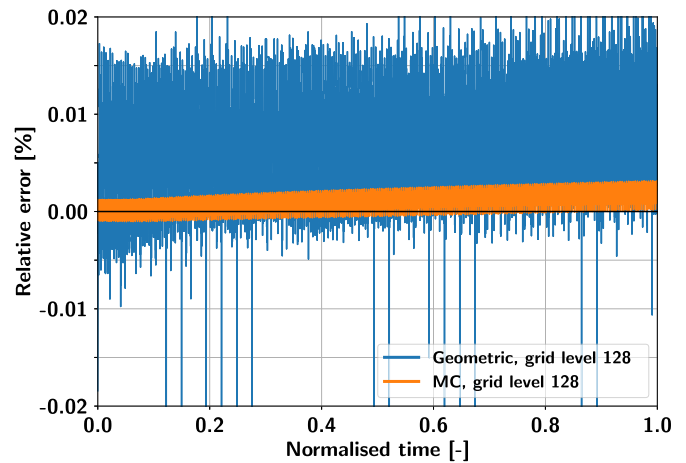


Fig. A29. Relative error of total interfacial area for a 2D circle advected in the diagonal direction as a function of normalised time. Grid resolution measured in the approximate number of cells per circle diameter N is equal to 128.

References

- [1] C.R. Kharangate, I. Mudawar, Review of computational studies on boiling and condensation, *Int. J. Heat Mass Transf.* 108 (2017) 1164–1196, doi:10.1016/j.ijheatmasstransfer.2016.12.065.
- [2] C. Hirt, B. Nichols, Volume of fluid (VOF) method for the dynamics of free boundaries, *J. Comput. Phys.* 39 (1) (1981) 201–225, doi:10.1016/0021-9991(81)90145-5.
- [3] W.F. Noh, P. Woodward, Slic (simple line interface calculation), in: A.I. van de Vooren, P.J. Zandbergen (Eds.), *Proceedings of the Fifth International Conference on Numerical Methods in Fluid Dynamics*, June 28–July 2, 1976, Twente University, Enschede, Springer Berlin Heidelberg, Berlin, Heidelberg, 1976, pp. 330–340.
- [4] D. Youngs, Time-dependent multi-material flow with large fluid distortion, in: K. Morton, M. Baines (Eds.), *Numerical Methods for Fluid Dynamics*, Academic Press, 1982, pp. 273–285.
- [5] M. Sussman, P. Smereka, S. Osher, A level set approach for computing solutions to incompressible two-phase flow, *J. Comput. Phys.* 114 (1) (1994) 146–159, doi:10.1006/jcph.1994.1155.
- [6] S. Popinet, Numerical models of surface tension, *Annu. Rev. Fluid Mech.* 50 (1) (2018) 49–75, doi:10.1146/annurev-fluid-122316-045034.
- [7] S.W.J. Welch, J. Wilson, A volume of fluid based method for fluid flows with phase change, *J. Comput. Phys.* 160 (2) (2000) 662–682, doi:10.1006/jcph.2000.6481.
- [8] S.W.J. Welch, T. Rachidi, Numerical computation of film boiling including conjugate heat transfer, *Numer. Heat Transf. Part B* 42 (1) (2002) 35–53, doi:10.1080/10407790190053824.
- [9] D.K. Agarwal, S.W.J. Welch, G. Biswas, F. Durst, Planar simulation of bubble growth in film boiling in near-critical water using a variant of the VOF method, *J. Heat Transf.* 126 (3) (2004) 329–338, doi:10.1115/1.1737779.
- [10] J.B. Haelssig, A.Y. Tremblay, J. Thibault, S.G. Etamad, Direct numerical simulation of interphase heat and mass transfer in multicomponent vapour-liquid flows, *Int. J. Heat Mass Transf.* 53 (19) (2010) 3947–3960, doi:10.1016/j.ijheatmasstransfer.2010.05.013.
- [11] K. Ling, Z.-Y. Li, W.-Q. Tao, A direct numerical simulation for nucleate boiling by the VOF method, *Numer. Heat Transf. Part A* 65 (10) (2014) 949–971, doi:10.1080/10407782.2013.850971.
- [12] D. Sun, J. Xu, Q. Chen, Modeling of the evaporation and condensation phase-change problems with fluent, *Numer. Heat Transf. Part B* 66 (4) (2014) 326–342, doi:10.1080/10407790.2014.915681.
- [13] M.W. Akhtar, S.J. Kleis, A volume of fluid phase change model on adaptive octree grids, *J. ASTM Int.* 8 (3) (2011) 1–21, doi:10.1520/JAI103348.
- [14] M.W. Akhtar, S.J. Kleis, Boiling flow simulations on adaptive octree grids, *Int. J. Multiph. Flow* 53 (2013) 88–99, doi:10.1016/j.ijmultiphaseflow.2013.01.008.
- [15] I. Perez-Raya, S.G. Kandlikar, Discretization and implementation of a sharp interface model for interfacial heat and mass transfer during bubble growth, *Int. J. Heat Mass Transf.* 116 (2018) 30–49, doi:10.1016/j.ijheatmasstransfer.2017.08.106.
- [16] I. Perez-Raya, S.G. Kandlikar, Numerical models to simulate heat and mass transfer at sharp interfaces in nucleate boiling, *Numer. Heat Transf. Part A* 74 (10) (2018) 1583–1610, doi:10.1080/10407782.2018.1543918.
- [17] L. Malan, *Direct Numerical Simulation of Free-surface and Interfacial Flow Using the VOF Method : Cavitating Bubble Clouds and Phase Change*, Université Pierre et Marie Curie - Paris VI, 2017 Thesis.
- [18] L. Malan, A. Malan, S. Zaleski, P. Rousseau, A geometric VOF method for interface resolved phase change and conservative thermal energy advection, *J. Comput. Phys.* 426 (2021) 109920, doi:10.1016/j.jcp.2020.109920.

- [19] Y. Sato, B. Niceno, A sharp-interface phase change model for a mass-conservative interface tracking method, *J. Comput. Phys.* 249 (2013) 127–161, doi:[10.1016/j.jcp.2013.04.035](https://doi.org/10.1016/j.jcp.2013.04.035).
- [20] N. Scapin, P. Costa, L. Brandt, A volume-of-fluid method for interface-resolved simulations of phase-changing two-fluid flows, *J. Comput. Phys.* 407 (2020) 109251, doi:[10.1016/j.jcp.2020.109251](https://doi.org/10.1016/j.jcp.2020.109251).
- [21] Y. Sato, B. Ničeno, Nucleate pool boiling simulations using the interface tracking method: Boiling regime from discrete bubble to vapor mushroom region, *Int. J. Heat Mass Transf.* 105 (2017) 505–524, doi:[10.1016/j.ijheatmasstransfer.2016.10.018](https://doi.org/10.1016/j.ijheatmasstransfer.2016.10.018).
- [22] L. Bureš, Y. Sato, Direct numerical simulation of phase change in the presence of non-condensable gases, *Int. J. Heat Mass Transf.* 151 (2020) 119400, doi:[10.1016/j.ijheatmasstransfer.2020.119400](https://doi.org/10.1016/j.ijheatmasstransfer.2020.119400).
- [23] Y. Sato, B. Ničeno, A new contact line treatment for a conservative level set method, *J. Comput. Phys.* 231 (10) (2012) 3887–3895, doi:[10.1016/j.jcp.2012.01.034](https://doi.org/10.1016/j.jcp.2012.01.034).
- [24] G. Weymouth, D.K.-P. Yue, Conservative volume-of-fluid method for free-surface simulations on cartesian-grids, *J. Comput. Phys.* 229 (8) (2010) 2853–2865, doi:[10.1016/j.jcp.2009.12.018](https://doi.org/10.1016/j.jcp.2009.12.018).
- [25] J. Schlottkke, B. Weigand, Direct numerical simulation of evaporating droplets, *J. Comput. Phys.* 227 (10) (2008) 5215–5237, doi:[10.1016/j.jcp.2008.01.042](https://doi.org/10.1016/j.jcp.2008.01.042).
- [26] K. Eisenschmidt, M. Ertl, H. Goma, C. Kieffer-Roth, C. Meister, P. Rauschenberger, M. Reitzle, K. Schlottke, B. Weigand, Direct numerical simulations for multiphase flows: An overview of the multiphase code FS3D, *Appl. Math. Comput.* 272 (2016) 508–517, doi:[10.1016/j.amc.2015.05.095](https://doi.org/10.1016/j.amc.2015.05.095).
- [27] D. Bothe, S. Fleckenstein, A volume-of-fluid-based method for mass transfer processes at fluid particles, *Chem. Eng. Sci.* 101 (2013) 283–302, doi:[10.1016/j.ces.2013.05.029](https://doi.org/10.1016/j.ces.2013.05.029).
- [28] L. Bureš, Y. Sato, Sharp-interface phase-change model with the VOFmethod, in: *Proceedings of the 5th Thermal and Fluids Engineering Conference (TFEC 2020)*, 2020, pp. 63–66, doi:[10.1615/TFEC2020.cmd.031939](https://doi.org/10.1615/TFEC2020.cmd.031939).
- [29] S. Bna, A. Cervone, V. Le Chenadec, S. Manservigi, R. Scardovelli, Review of split and unsplit geometric advection algorithms, *AIP Conf. Proc.* 1558 (1) (2013) 875–878, doi:[10.1063/1.4825636](https://doi.org/10.1063/1.4825636).
- [30] J.E. Pilliod, E.G. Puckett, Second-order accurate volume-of-fluid algorithms for tracking material interfaces, *J. Comput. Phys.* 199 (2) (2004) 465–502, doi:[10.1016/j.jcp.2003.12.023](https://doi.org/10.1016/j.jcp.2003.12.023).
- [31] E. Aulisa, S. Manservigi, R. Scardovelli, S. Zaleski, Interface reconstruction with least-squares fit and split advection in three-dimensional cartesian geometry, *J. Comput. Phys.* 225 (2) (2007) 2301–2319, doi:[10.1016/j.jcp.2007.03.015](https://doi.org/10.1016/j.jcp.2007.03.015).
- [32] J. López, C. Zanzi, P. Gómez, R. Zamora, F. Faura, J. Hernández, An improved height function technique for computing interface curvature from volume fractions, *Comput. Methods Appl. Mech. Eng.* 198 (33) (2009) 2555–2564, doi:[10.1016/j.cma.2009.03.007](https://doi.org/10.1016/j.cma.2009.03.007).
- [33] G.Y. Soh, G.H. Yeoh, V. Timchenko, An algorithm to calculate interfacial area for multiphase mass transfer through the volume-of-fluid method, *Int. J. Heat Mass Transf.* 100 (2016) 573–581, doi:[10.1016/j.ijheatmasstransfer.2016.05.006](https://doi.org/10.1016/j.ijheatmasstransfer.2016.05.006).
- [34] W.E. Lorensen, H.E. Cline, Marching cubes: a high resolution 3D surface construction algorithm, in: *Proceedings of the 14th Annual Conference on Computer Graphics and Interactive Techniques, SIGGRAPH '87 (Anaheim, CA)*, 249, 1987, pp. 163–169, doi:[10.1145/37401.37422](https://doi.org/10.1145/37401.37422).
- [35] A.J. Chorin, Numerical solution of the Navier–Stokes equations, *Math. Comput.* 22 (1968) 745–762, doi:[10.1090/S0025-5718-1968-0242392-2](https://doi.org/10.1090/S0025-5718-1968-0242392-2).
- [36] Y. Saad, *Iterative Methods for Sparse Linear Systems*, SIAM, 2003.
- [37] J.U. Brackbill, D.B. Kothe, C. Zemach, A continuum method for modeling surface tension, *J. Comput. Phys.* 100 (1992) 335–354, doi:[10.1016/0021-9991\(92\)90240-Y](https://doi.org/10.1016/0021-9991(92)90240-Y).
- [38] F.H. Harlow, J.E. Welch, Numerical calculation of time-dependent viscous incompressible flow of fluid with free surface, *Phys. Fluids* 8 (12) (1965) 2182–2189, doi:[10.1063/1.1761178](https://doi.org/10.1063/1.1761178).
- [39] P.L. Roe, Characteristic-based schemes for the euler equations, *Annu. Rev. Fluid Mech.* 18 (1) (1986) 337–365, doi:[10.1146/annurev.fl.18.010186.002005](https://doi.org/10.1146/annurev.fl.18.010186.002005).
- [40] S. Osher, R. Fedkiw, *Level Set Methods and Dynamic Implicit Surfaces*, Springer New York, New York, NY, 2003, doi:[10.1007/0-387-22746-6_8](https://doi.org/10.1007/0-387-22746-6_8).
- [41] D. Koutsoyiannis, Clausius–Clapeyron equation and saturation vapour pressure: simple theory reconciled with practice, *Eur. J. Phys.* 22 (2012) 295–305, doi:[10.1088/0143-0807/33/2/295](https://doi.org/10.1088/0143-0807/33/2/295).
- [42] G.W. Thomson, The Antoine equation for vapor-pressure data, *Chem. Rev.* 38 (1) (1946) 1–39 PMID: 21016992, doi:[10.1021/cr60119a001](https://doi.org/10.1021/cr60119a001).
- [43] G. Son, V.K. Dhir, Numerical simulation of film boiling near critical pressures with a level set method, *J. Heat Transf.* 120 (1) (1998) 183–192, doi:[10.1115/1.2830042](https://doi.org/10.1115/1.2830042).
- [44] C. Kunkelmann, P. Stephan, CFD simulation of boiling flows using the volume-of-fluid method within openfoam, *Numer. Heat Transf. Part A* 56 (8) (2009) 631–646, doi:[10.1080/10407780903423908](https://doi.org/10.1080/10407780903423908).
- [45] L. Scriven, On the dynamics of phase growth, *Chem. Eng. Sci.* 10 (1) (1959) 1–13, doi:[10.1016/0009-2509\(59\)80019-1](https://doi.org/10.1016/0009-2509(59)80019-1).
- [46] L. Florschuetz, C. Henry, A. Khan, Growth rates of free vapor bubbles in liquids at uniform superheats under normal and zero gravity conditions, *Int. J. Heat Mass Transf.* 12 (11) (1969) 1465–1489, doi:[10.1016/0017-9310\(69\)90028-3](https://doi.org/10.1016/0017-9310(69)90028-3).
- [47] X. Qu, M. Tian, G. Zhang, X. Leng, Experimental and numerical investigations on the air-steam mixture bubble condensation characteristics in stagnant cool water, *Nucl. Eng. Des.* 285 (2015) 188–196, doi:[10.1016/j.nucengdes.2014.12.031](https://doi.org/10.1016/j.nucengdes.2014.12.031).
- [48] H. Kalman, Condensation of bubbles in miscible liquids, *Int. J. Heat Mass Transf.* 46 (18) (2003) 3451–3463, doi:[10.1016/S0017-9310\(03\)00128-5](https://doi.org/10.1016/S0017-9310(03)00128-5).
- [49] E.W. Lemmon, M.O. McLinden, D.G. Friend, Thermophysical properties of fluid systems, in: P.J. Linstrom, W.G. Mallard (Eds.), *NIST Chemistry WebBook, NIST Standard Reference Database Number 69*, National Institute of Standards and Technology, 2018, doi:[10.18434/T4D303](https://doi.org/10.18434/T4D303), [Accessed 31.7.2020]
- [50] H. Jia, X. Xiao, Y. Kang, Investigation of bubble behavior with phase change under the effect of noncondensable gas, *Chem. Eng. Sci.* 207 (2019) 631–643, doi:[10.1016/j.ces.2019.07.003](https://doi.org/10.1016/j.ces.2019.07.003).
- [51] E. Sanjari, M. Honarmand, H. Badihi, A. Ghaheri, An accurate generalized model for predict vapor pressure of refrigerants, *Int. J. Refrig.* 36 (4) (2013) 1327–1332, doi:[10.1016/j.ijrefrig.2013.01.007](https://doi.org/10.1016/j.ijrefrig.2013.01.007).
- [52] P. Lu, X. Zheng, P. Yang, L. Fang, H. Huang, Numerical investigation into the vapor-liquid flow in the mixer of a liquid metal magneto-hydro-dynamic system, *RSC Adv.* 7 (57) (2017) 35765–35770, doi:[10.1039/c7ra06135h](https://doi.org/10.1039/c7ra06135h).
- [53] E.N. Fuller, P.D. Schettler, J.C. Giddings, A new method for prediction of binary gas-phase coefficients, *Ind. Eng. Chem.* 58 (5) (1966) 18–27, doi:[10.1021/ie50677a007](https://doi.org/10.1021/ie50677a007).
- [54] E.N. Fuller, K. Ensley, J.C. Giddings, Diffusion of halogenated hydrocarbons in helium. the effect of structure on collision cross sections, *J. Phys. Chem.* 73 (11) (1969) 3679–3685, doi:[10.1021/j100845a020](https://doi.org/10.1021/j100845a020).
- [55] D. Legendre, R. Zenit, J.R. Velez-Cordero, On the deformation of gas bubbles in liquids, *Phys. Fluids* 24 (4) (2012) 043303, doi:[10.1063/1.4705527](https://doi.org/10.1063/1.4705527).
- [56] Y. Lerner, H. Kalman, R. Letan, Condensation of an accelerating-decelerating bubble: experimental and phenomenological analysis, *J. Heat Transf.* 109 (2) (1987) 509–517, doi:[10.1115/1.3248112](https://doi.org/10.1115/1.3248112).
- [57] W.E. Ranz, W.R. Marshall, *Evaporation from drops*, *Chem. Eng. Prog.* 48 (3) (1952) 141–146.
- [58] Y. Chen, F. Mayinger, Measurement of heat transfer at the phase interface of condensing bubbles, *Int. J. Multiph. Flow* 18 (6) (1992) 877–890, doi:[10.1016/0301-9322\(92\)90065-O](https://doi.org/10.1016/0301-9322(92)90065-O).
- [59] S. Al Issa, P. Weisensee, R. Macián-Juan, Experimental investigation of steam bubble condensation in vertical large diameter geometry under atmospheric pressure and different flow conditions, *Int. J. Heat Mass Transf.* 70 (2014) 918–929, doi:[10.1016/j.ijheatmasstransfer.2013.11.049](https://doi.org/10.1016/j.ijheatmasstransfer.2013.11.049).
- [60] J.C. Cano-Lozano, C. Martínez-Bazán, J. Magnaudet, J. Tchoufag, Paths and wakes of deformable nearly spherical rising bubbles close to the transition to path instability, *Phys. Rev. Fluids* 1 (2016) 053604, doi:[10.1103/PhysRevFluids.1.053604](https://doi.org/10.1103/PhysRevFluids.1.053604).
- [61] Lubomír Bureš, Yohei Sato, Andreas Pautz, Piecewise linear interface-capturing volume-of-fluid method in axisymmetric cylindrical coordinates, *Journal of Computational Physics* (2021) 110291 In press, doi:[10.1016/j.jcp.2021.110291](https://doi.org/10.1016/j.jcp.2021.110291).